Chemical Science

ROYAL SOCIETY OF CHEMISTRY

REVIEW

View Article Online
View Journal | View Issue

Cite this: *Chem. Sci.*, 2022, **13**, 3942

Metal oxyhalides: an emerging family of nonlinear optical materials

Xinglong Chen * and Kang Min Ok *

Second-order nonlinear optical (NLO) materials have drawn enormous academic and technological attention attributable to their indispensable role in laser frequency conversion and other greatly facilitated applications. The exploration of new NLO materials with high performances thus has long been an intriguing research field for chemists and material scientists. However, an ideal NLO material should simultaneously satisfy quite a few fundamental yet rigorous criteria including a noncentrosymmetric structure, large NLO coefficients, desired transparent range, large birefringence, high laser damage threshold, and availability of a large-size single crystal. Therefore, the identification of promising compound systems, targeted design, and experience-based syntheses are crucial to discover novel NLO materials working in the spectral region of interest. As an important family of mixed-anion compounds, versatile metal oxyhalides containing metal-centered oxyhalide functional units ($[MO_mX_n]$ (X = F, Cl, Br, and I)) are becoming a marvelous branch for interesting NLO materials. Especially, when the central metals are d^0/d^{10} transition metals or heavy post-transition metals, a number of novel NLO materials with superior functionalities are expected. Our thorough review on the recent achievements of metal oxyhalides for NLO materials are divided into the fast-growing NLO metal oxyhalides with single type halogen anions and the newly identified NLO metal oxyhalides with mixed halogen anions. Here we mainly focus on the design strategy, structural chemistry, NLO-related properties, and structure–property correlation of the metal oxyhalides with relatively large NLO responses. We hope this review can provide an insight on the rational design and future development of emerging metal oxyhalides for NLO and other applications.

Received 22nd December 2021
Accepted 14th March 2022

DOI: 10.1039/d1sc07121a

rsc.li/chemical-science

Department of Chemistry, Sogang University, 35 Baekbeom-ro, Mapo-gu, Seoul 04107, Korea. E-mail: kmok@sogang.ac.kr; xinglong.chen@anl.gov

Dr Xinglong Chen received his BS degree from Shandong University and PhD degree from the University of Chinese Academy of Sciences in 2018 guided by Professor Shilie Pan for the study of new nonlinear optical (NLO) materials and birefringent materials. Subsequently, he joined Professor Kang Min Ok's group in Korea as a postdoctoral researcher, working on the exploration of new NLO materials and large single crystal growth. Currently, he has been working at Argonne National Laboratory, USA, since 2021, and his current research focuses on high-quality single crystal growth of quantum materials and the study of their exotic electronic/magnetic behaviors.

Professor Kang Min Ok attended Sogang University, Korea, earning BS and MS degrees in Chemistry, followed by a PhD from the University of Houston, USA, guided by Professor P. Shiv Halasyamani. He performed postdoctoral research in the group of Professor Dermot O'Hare at the University of Oxford, UK. Professor Ok worked as a distinguished scholar at Chung-Ang University (CAU), Korea. Currently, he is a Professor at Sogang University, Korea. His research includes discovering novel functional solid-state materials with noncentrosymmetric structures. Professor Ok has authored over 230 scientific publications to date.

1. Introduction

The second-order nonlinear optical (NLO) phenomenon, *i.e.*, second-harmonic generation (SHG) characterized by the frequency-doubling effect, was first observed by Franken and coworkers during the laser applying experiment on a non-centrosymmetric (NCS) quartz soon after the invention of the laser, an unprecedented coherent light source with single-frequency and ultra-high irradiance.[1] Since then, a variety of NLO materials that can constructively expand the wavelengths of lasers have been greatly promoting the development of laser science and other numerous scientific and technological fields.[2,3] Therefore, the development of superior performing NLO materials has been attracting immense interest. A few widely used NLO crystals include $AgGaS_2$ (AGS),[4] $AgGaSe_2$ (AGSe),[5] $ZnGeP_2$ (ZGP),[6] $KTiOPO_4$ (KTP),[7] $LiNbO_3$ (LN),[8] KH_2PO_4 (KDP),[9] β-BaB_2O_4 (BBO),[10] LiB_3O_5 (LBO),[11] $CsLiB_6O_{10}$ (CLBO),[12] and $KBe_2BO_3F_2$ (KBBF).[13] Among them, only the "oxygen-free" crystals such as AGS, AGSe, and ZGP are applicable to the mid-infrared (mid-IR) spectral region (3–20 μm) owing to their superior IR transparent range (≥12 μm) and robust NLO effects. Unfortunately, however, their applications have been fiercely restricted by some intrinsic flaws such as an inadequate laser damage threshold (LDT) for AGS, harmful two photon absorption for ZGP, and nonphase-matching behavior for AGSe.[14] Meanwhile, KBBF has been considered to be a very good NLO material working in the deep-ultraviolet (deep-UV) region (<200 nm). However, growing large crystals of KBBF is very difficult attributed to its severely layering growth habit.[15] In addition, NLO materials operating in the visible–near-infrared (Vis–NIR) region (400–2000 nm) were relatively satisfactory although strong SHG responses combined with high LDTs are still a very important requirement in this region.

Admittedly, the exploration of high-performance NLO materials is extremely challenging considering that several essential yet rigorous criteria should be fulfilled simultaneously in an NLO compound for practical applications. A few critical criteria include, but are not limited to, the following. (1) The single crystal form of the compound should be optically transparent in the working spectral range to ensure the output of the generated coherent light. (2) The material should crystallize in an NCS space group that can have non-zero second-order NLO coefficients. (3) Critical for the stabilized output of laser, the compound should possess a relatively large birefringence ($\Delta n = n_z - n_x$). (4) The single crystal form of the material is preferred to have a high LDT to avoid damage under laser irradiation, particularly considering the urgent demands of high-power lasers. (5) Bulk single crystals with high optical quality and desired sizes (>5 mm × 5 mm × 5 mm) are needed for further characterizations such as NLO coefficients, refractive indices, phase-matching angle and range, *etc.*, and the fabrication of NLO devices. Here we would like to give some detailed explanations for the above-mentioned criteria. For criterion (2), note that the NCS space groups belonging to one of the following point groups, 432, 422 and 622 should be excluded for NLO compounds because they inherently possess second-order NLO coefficients of zero under Neumann's principle or Kleinman's conditions. In fact, large NLO coefficients are undoubtedly preferred to achieve a high laser conversion efficiency. Generally, compounds that crystallize in polar point groups (1, 2, 3, 4, 6, *m*, *mm*2, 3*m*, 4*mm* and 6*mm*) with large polarity are desired although some exceptions of large NLO responses exist in NCS compounds with nonpolar point groups. For criterion (3), a relatively large birefringence is necessary to achieve the so-called "phase-matching" condition that is usually realized by birefringence matching during the laser frequency conversion processes. For instance, in a common NLO application such as SHG (frequency-doubling), the phase-matching condition occurs when the refractive index of the incident light [$n(\omega)$] is equal to that of the SHG light [$n(2\omega)$], *i.e.*, $n(\omega) = n(2\omega)$. However, if the birefringence of a crystal is too small, the $n(\omega)$ and $n(2\omega)$ curves would never intersect, and phase-matching cannot occur (note that the refractive indices change as a function of light frequency). Otherwise, a large birefringence can attain the "$n(\omega) = n(2\omega)$" condition, *i.e.*, phase-matching, in a wide wavelength (frequency) range.[16] This phase-matchable wavelength range further confines the working spectral range of an NLO crystal firstly constrained by its transparent range. For criterion (4), as materials with large band gaps tend more likely to prevent the laser-induced damage, NLO crystals with large band gaps are normally pursued, which is consistent with criterion (1) where large band gaps are needed to ensure a wide transparent range in the UV side of the transparent windows, although the definition of "large" varies considerably depending on the practical working wavelengths of NLO materials (see below). Moreover, some of the parameters in the above-mentioned requirements are inversely correlated. For example, the inverse relationship between the band gap and SHG response[17] makes it more difficult to obtain a superb NLO material with balanced overall performance. It should be noted that the more detailed requirements for SHG response, LDT, and band gap vary for the NLO materials according to their working spectral regions and other specific purposes. For instance, an ideal mid-IR NLO material is preferred to have a larger band gap (>2.62 eV) than those of the commercial NLO materials (*e.g.*, AGS, AGSe, ZGP), a larger LDT than that of AGS (30 MW cm^{-2}), a comparable NLO response to that of AGS [at least ≥0.5× AGS (13 pm V^{-1})], and wide IR transparency (usually >5 μm, ideally >10 μm). An ideal Vis–NIR NLO material should have a strong SHG response comparable to that of KTP [≥0.5× KTP (3.7 pm V^{-1})] and a band gap larger than that of KTP (>3.54 eV). For an ideal DUV NLO material, a much wider band gap (>6.2 eV) and an SHG response larger than that of KDP (0.39 pm V^{-1}) are required.

In this context, numerous efforts have been made to design and synthesize new inorganic NLO materials,[18] which include the exploration of metal chalcogenides[19] and metal halides[20] for mid-IR NLO materials, various oxide-based metal salts for UV and Vis–NIR NLO materials,[21] and fluorooxoborates[22] and fluorophosphates[23] for deep-UV NLO materials. Notably, the study of mixed-anion compounds such as metal oxyhalides,[24] metal chalcogenide halides,[25] and metal oxysulfides[26] has shone light on the development of many NLO materials. Among them, the

emerging NLO metal oxyhalides have recently received growing interest. Broadly speaking, metal oxyhalides refer to all compounds containing metal-centered oxyhalide groups, $[MO_mX_n]$ (X = F, Cl, Br, and I). Especially, the $[MO_mX_n]$ units act as important functional building blocks (FBBs), although the metal oxyhalides with additional anionic groups (*e.g.*, $[BO_3]$) are usually identified as metal salt halides. In the $[MO_mX_n]$ group, the metal cation is coordinated by at least two types of multiple anions such as O^{2-} and X^- rather than a single type of anion. Materials containing central metals of $[MO_mX_n]$ belonging to the d^0/d^{10} transition metals or heavy post-transition metals manifesting second-order Jahn–Teller (SOJT) distortions are of particular interest.[27] The SOJT distortions of $[MO_mX_n]$ groups can induce large local asymmetry, which would be superimposed to large macroscopic asymmetry when the $[MO_mX_n]$ groups are well-aligned. Therefore, the formed metal–oxyhalide polyhedra can be preferable FBBs for the design and discovery of novel NLO materials, owing to their asymmetric characteristics that have natural advantages in producing NCS structures, strong SHG effects, as well as large optical anisotropies (birefringences). Consequently, there has been rising consciousness that metal oxyhalides can be a marvelous branch for the exploration of high-performance NLO materials.

Herein, we give a brief retrospect of the recently discovered metal oxyhalides that exhibit intriguing NLO properties. In this review, the metal oxyhalides are divided into two categories: the first category is the classic NLO metal oxyhalides that only contain single type halogen anions, including those with additional NLO-active anionic groups (*e.g.*, $[BO_3]$, $[BO_4]$, $[CH_3COO]$, $[NO_3]$, $[VO_4]$, $[SeO_3]$, $[IO_3]$) which are characterized by proved direct contributions to NLO responses of materials owing to their considerable local asymmetry, as well as the so-called "pure" metal oxyhalides without additional anionic groups. The other one is the newly emerged NLO metal oxyhalides with more than one type of halogen anions. Among the metal cations that form the oxyhalide polyhedra, only d^0/d^{10} transition metal cations (Ti^{4+}, V^{5+}, Mo^{6+}, Zn^{2+}, Cd^{2+}, *etc.*) and post-transition metal cations (Pb^{2+}, Bi^{3+}, Sn^{2+}, *etc.*) are included. In addition, we are mainly focusing on the cases in which the $[MO_mX_n]$ groups make considerable contributions to SHG responses. The examination contains material design strategies, structures, syntheses, structure-driven NLO-related properties, and structure–property correlation. We also make a broader comparison of the discussed NLO metal oxyhalides and provide a perspective on the future development of metal oxyhalide NLO materials.

2. NLO metal oxyhalides with single type halogen anions

2.1 NLO metal oxyhalides with additional anionic groups

2.1.1 NLO metal oxyhalide borates

Pb_2BO_3X (X = Cl, Br, and I). Crystallizing in the trigonal NCS space group, *P*321, the isostructural Pb_2BO_3Cl,[28] Pb_2BO_3Br,[29] and Pb_2BO_3I[30] belong to the KBBF family. Although the structures of Pb_2BO_3X have been described as cationic $[Pb_2BO_3]^+$ layers and interlayered X^- anions in the literature, here we would provide an alternative structural description for the materials in terms of metal–oxyhalides. The structures are constructed from Pb–oxyhalide polyhedral groups, $[PbO_3X_2]$, shared by well-arranged $[BO_3]$ trigonal planar units through oxygen atoms (Fig. 1). Single crystals of Pb_2BO_3Cl were grown from the melt of stoichiometric mixtures of PbO, $PbCl_2$, and H_3BO_3 through a high temperature reaction in a sealed silica tube. However, single crystals of Pb_2BO_3Br and Pb_2BO_3I were grown *via* mild hydrothermal reactions by using PbO, $PbCl_2$, H_3BO_3, and H_2O, possibly attributable to the decreased thermostability of Pb_2BO_3Br and Pb_2BO_3I caused by the volatility of the corresponding halide anions. Pb_2BO_3Cl melts congruently with a melting point of 630 °C, whereas Pb_2BO_3Br and Pb_2BO_3I decompose before melting. The SHG responses of Pb_2BO_3Cl, Pb_2BO_3Br, and Pb_2BO_3I are 9×, 9.5×, and 10× KDP, respectively, which are among the largest in the KBBF family. The remarkable SHG responses should be attributed to the synergistic effects of the $[PbO_3X_2]$ and coplanar arranged $[BO_3]$ NLO-active groups. It should be noticed that Pb_2BO_3Cl possesses many excellent properties for a promising NLO material in the Vis–NIR region, which include considerable SHG efficiency, sufficient birefringence (0.12@1064 nm), the largest band gap (3.99 eV) in the family, the highest thermostability, and facile growth of large crystals thanks to the congruently melting behavior.

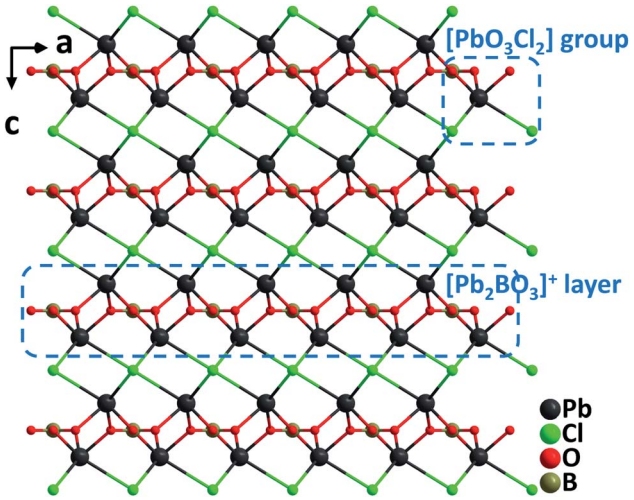

Fig. 1 Crystal structure of Pb_2BO_3Cl viewed along the *b*-axis.

$Pb_2B_5O_9X$ (X = Cl, Br, and I). Isomorphic $Pb_2B_5O_9X$ (X = Cl, Br, and I), crystallizing in the orthorhombic polar space group *Pnn*2, belong to the derivatives of the hilgardite structure.[31] Different from the isolated $[BO_3]$ group in Pb_2BO_3X, $[BO_3]$ and $[BO_4]$ are polymerized to form a 3D open-framework of zeolitic $[B_5O_9]_\infty$ in $Pb_2B_5O_9X$ (Fig. 2). Pb^{2+} cations are coordinated by O^{2-} and X^- to form distorted Pb–oxyhalide polyhedra, $[PbO_7X_2]$, which are further connected to the $[B_5O_9]_\infty$ framework by bridging O atoms. Remarkably, the $[PbO_7I_2]$ polyhedra in $Pb_2B_5O_9I$ exhibit significantly larger SOJT distortions than those of $[PbO_7Cl_2]$ and $[PbO_7Br_2]$ polyhedra in $Pb_2B_5O_9Cl$ and

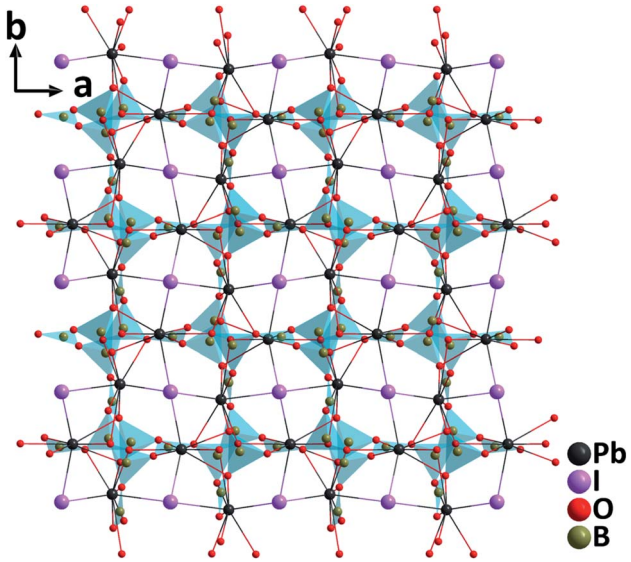

Fig. 2 Crystal structure of $Pb_2B_5O_9I$ viewed along the *c*-axis.

$Pb_2B_5O_9Br$, respectively, possibly attributed to the increased electronegativity difference between the coordinated O^{2-} and I^-. As a result, $Pb_2B_5O_9I$ reveals a much stronger powder SHG response (13.5× KDP) than $Pb_2B_5O_9Cl$ (4× KDP) and $Pb_2B_5O_9Br$ (4.7× KDP). Theoretical analyses indicate that the increased cooperation of all the constituting units such as Pb^{2+}, I^-, and B–O groups is responsible for the outstanding SHG response of $Pb_2B_5O_9I$, which is the largest among borates. The band gaps of $Pb_2B_5O_9Cl$, $Pb_2B_5O_9Br$, and $Pb_2B_5O_9I$ are measured to be 3.72, 3.54, and 3.33 eV, respectively, following the usual band gap trend for halides. It is noteworthy that, a large single crystal of $Pb_2B_5O_9Cl$ ($25 \times 6 \times 2$ mm^3) has been successfully grown by a high temperature solution method using the $PbCl_2$–B_2O_3 flux system.[31d] In addition to the above compounds, the NLO properties of $CsZn_2BO_3X_2$ (X = F and Cl)[32] containing $[ZnO_3X]$ oxyhalide groups are also summarized in Table 1.

2.1.2 NLO metal oxyhalide acetates

$Cs_3Pb_2(CH_3COO)_2X_5$ (X = Br and I). Recently, $Cs_3Pb_2(CH_3COO)_2X_5$ (X = Br and I) have been successfully synthesized by incorporating acetate groups into lead halide perovskites with the aid of a facile solvothermal method.[33] Noticeably, large crystals up to 8 mm long with the needle-like growth habit could be easily grown. Isostructural $Cs_3Pb_2(CH_3COO)_2X_5$ crystallize in the polar orthorhombic space group, *Amm*2, featuring highly oriented $[Pb_2(CH_3COO)_2X_5]$ anionic chains constructed from severely distorted $[PbO_2X_4]$ polyhedra and asymmetric $[CH_3COO]$ groups (Fig. 3). In the $[PbO_2X_4]$ polyhedra, the Pb–O distances are much shorter than Pb–X lengths while lone electron pair effects are obviously observed. These highly distorted $[PbO_2X_4]$ polyhedra are favorable to produce large polarizability and anisotropy. Correspondingly, $Cs_3Pb_2(CH_3COO)_2Br_5$ and $Cs_3Pb_2(CH_3COO)_2I_5$ reveal remarkable phase-matching SHG responses of 4× and 8× KDP, respectively, as well as large birefringences of 0.15 and 0.26 at 1064 nm, respectively. Dipole moment calculations indicate that although the polarizations of $[PbO_2X_4]$ polyhedra are opposite to those of $[CH_3COO]$ groups along the polar *c*-axis, the net dipole moments in the unit cells are still large owing to the predominant contribution of $[PbO_2X_4]$ groups. Therefore, the highly distorted $[PbO_2X_4]$ polyhedra should be responsible for the strong SHG responses. Besides, the enhanced SHG of $Cs_3Pb_2(CH_3COO)_2I_5$ compared to that of $Cs_3Pb_2(CH_3COO)_2Br_5$ can be explained by the corrected total dipole moment, which is inversely correlated with the volume and the square of band gaps. As is well known that the substitution of I for Br results in the decrease of the band gap, the experimental band gap of $Cs_3Pb_2(CH_3COO)_2I_5$ (2.55 eV) is smaller than that of $Cs_3Pb_2(CH_3COO)_2Br_5$ (3.26 eV).

$Rb_3Pb_2(CH_3COO)_2X_5$ (X = Br and Cl). Through equivalent substitution of alkali metal cations and halogen anions based on $Cs_3Pb_2(CH_3COO)_2X_5$ (X = Br and I), two new crystals of $Rb_3Pb_2(CH_3COO)_2X_5$ (X = Br and Cl) were successfully synthesized by solvothermal reactions.[34] Although isostructural to $Cs_3Pb_2(CH_3COO)_2Br_5$, $Rb_3Pb_2(CH_3COO)_2Br_5$ exhibits a larger birefringence (0.18@1064 nm), a stronger SHG response (6× KDP), and a relatively large band gap (3.12 eV), demonstrating that the replacement of alkali metal cations could improve the NLO properties. Meanwhile, for $Rb_3Pb_2(CH_3COO)_2Cl_5$, the substitution of Cl^- for Br^- anions leads to a larger band gap (3.64 eV), the broader UV transmittance (down to 287 nm), and the higher LDT.

2.1.3 NLO metal oxyhalide nitrates

$Bi_6O_6F_5(NO_3)$. $Bi_6O_6F_5(NO_3)$ crystallizes in the polar NCS space group, *R*3.[35] It features a double layered structure, which consists of asymmetric $[BiO_3F_2]$ polyhedra, $[NO_3]^-$ trigonal planar groups, and isolated F^- anions (Fig. 4). In the highly unsymmetrical $[BiO_3F_2]$ polyhedra containing lone pairs, the Bi–O lengths are 2.13(3)–2.22(3) Å, whereas those of Bi–F are 2.433(2)–2.53(2) Å. The $[BiO_3F_2]$ polyhedra share the vertices to form a Bi-oxyfluoride double layer in the *ab*-plane. In the interlayer space, $[NO_3]^-$ planar units are aligned in parallel with the Bi-oxyfluoride layers, which is achieved *via* the incorporation of F^- anions. The F^- anions in the interlayer inhibit the direct interactions between Bi^{3+} cations and O^{2-} in $[NO_3]^-$ anionic groups. The π-delocalized electrons around $[NO_3]^-$ units show significant interactions with lone pairs on the highly polarizable Bi^{3+} cations. Single crystals of $Bi_6O_6F_5(NO_3)$ were hydrothermally grown at 200 °C, and they are thermally stable up to 400 °C. Powder SHG measurements on polycrystalline $Bi_6O_6F_5(NO_3)$ reveal that the material possesses a relatively large SHG response (3× KDP) with phase-matchability under 1064 nm laser irradiation. Dipole moment analyses indicate that although $[BiO_3F_2]$ polyhedra have substantial local dipole moments, the net polarization of $[BiO_3F_2]$ polyhedra is largely reduced due to their antiparallel alignment. However, the SHG response should be attributed to the aligned $[NO_3]$ anion groups as well as the interactions between lone pairs on Bi^{3+} cations and π-delocalized electrons on $[NO_3]^-$ groups.

2.1.4 NLO metal oxyhalide vanadates

$Cs_2CdV_2O_6Cl_2$. The cadmium oxychloride vanadate containing d^0 (V^{5+}) and d^{10} (Cd^{2+}) cations, $Cs_2CdV_2O_6Cl_2$, was synthesized by using a high temperature solid state reaction at 550 °C.[36] The compound crystallizes in the polar NCS space

Table 1 Space groups, metal–oxyhalide unit types, and key properties of NLO metal oxyhalides with single type halogen anions

No.	Crystal	Space group	Metal–oxyhalide unit type	SHG[a]	E_g (eV)	Birefringence (calculated)	IR cutoff edge (μm)	LDT[d] (MW cm^{-2})
1	Pb_2BO_3Cl (ref. 28)	*P*321	$[PbO_3Cl_2]$	9× KDP	3.99	0.12@1064 nm	—	—
2	Pb_2BO_3Br (ref. 29)	*P*321	$[PbO_3Br_2]$	9.5× KDP	3.33	0.055@1064 nm	—	—
3	Pb_2BO_3I (ref. 30)	*P*321	$[PbO_3I_2]$	10× KDP	~3.45	0.036@1064 nm	—	—
4	$Pb_2B_5O_9Cl$ (ref. 31)	*Pnn*2	$[PbO_7Cl_2]$	4× KDP	3.77	—	6.80[b]	—
5	$Pb_2B_5O_9Br$ (ref. 31)	*Pnn*2	$[PbO_7Br_2]$	4.7× KDP	3.54	—	6.86[b]	—
6	$Pb_2B_5O_9I$ (ref. 31)	*Pnn*2	$[PbO_7I_2]$	13.5× KDP	3.1	—	6.96[b]	—
7	$CsZn_2BO_3F_2$ (ref. 32)	*R*32	$[ZnO_3F]$	2.8× KDP	>6.5	—	—	—
8	$CsZn_2BO_3Cl_2$ (ref. 32)	*R*32	$[ZnO_3Cl]$	3.2× KDP	>6.5	—	—	—
9	$Cs_3Pb_2(CH_3COO)_2Br_5$ (ref. 33)	*Amm*2	$[PbO_2Br_4]$	4× KDP	3.26	0.15@1064 nm	6.0[b]	66.2
10	$Cs_3Pb_2(CH_3COO)_2I_5$ (ref. 33)	*Amm*2	$[PbO_2I_4]$	8× KDP	2.55	0.26@1064 nm	—	43.4
11	$Rb_3Pb_2(CH_3COO)_2Br_5$ (ref. 34)	*Amm*2	$[PbO_2Br_4]$	6× KDP	3.12	0.18@1064 nm	6.0[b]	71.3
12	$Rb_3Pb_2(CH_3COO)_2Cl_5$ (ref. 34)	*Amm*2	$[PbO_2Cl_4]$	3× KDP	3.64	0.11@1064 nm	—	135.38
13	$Bi_6O_6F_5(NO_3)$ (ref. 35)	*R*3	$[BiO_3F_2]$	3× KDP	4.0	—	—	—
14	$Cs_2CdV_2O_6Cl_2$ (ref. 36)	*Cm*	$[CdO_2Cl_4]$	5× KDP	3.0	—	10.4[b]	—
15	$Cs_3CdV_4O_{12}Br$ (ref. 36)	*Cmm*2	$[CdO_4Br_2]$	7× KDP	3.13	—	10.4[b]	—
16	$BaBi(SeO_3)_2Cl$ (ref. 37)	$Cmc2_1$	$[BiO_8Cl]$	16× KDP	3.4	0.1@1064 nm	—	—
17	$BiFSeO_3$ (ref. 38)	$Pca2_1$	$[BiO_5F_2]$	13.5× KDP, 1.1× KTP	3.83	—	—	—
18	$RbTeMo_2O_8F$ (ref. 40)	*Pn*	$[MoO_5F]$	27× KDP, 2.2× KTP	3.63	0.263@546 nm	5.40[b]	—
19	$Cs(TiOF)_3(SeO_3)_2$ (ref. 42)	$P6_3mc$	$[TiO_4F_2]$	5× KDP	3.50	0.279@1064 nm	10[b]	—
20	$Bi_3(SeO_3)_3(Se_2O_5)F$ (ref. 43)	$P2_1$	$[BiO_6Cl]$	8× KDP	3.8	—	10[b]	—
21	$Ba(MoO_2F)_2(SeO_3)_2$ (ref. 44)	*Aba*2	$[MoO_5F]$	2.8× KDP[44a]/3× KDP[44b]	3.23 (ref. 44a)/3.30 (ref. 44b)	0.23 (ref. 44a)/0.18 (ref. 44b)@1064 nm	10[b]	126.3 (ref. 44b)
22	$Ba(MoO_2F)_2(TeO_3)_2$ (ref. 44)	*Aba*2	$[MoO_5F]$	7.8× KDP[44a]/4× KDP[44b]	2.96 (ref. 44a)/3.27 (ref. 44b)	0.23 (ref. 44a)/0.27 (ref. 44b)@1064 nm	10[b]	113.1 (ref. 44b)
23	$KBi_2(IO_3)_2F_5$ (ref. 45)	$P2_1$	$[BiO_2F_4]$	12× KDP	3.75	—	11[b]	—
24	$RbBi_2(IO_3)_2F_5$ (ref. 45)	$P2_1$	$[BiO_2F_4]$	9.5× KDP	3.78	—	11[b]	—
25	$CsBi_2(IO_3)_2F_5$ (ref. 45)	$P2_1$	$[BiO_2F_4]$	7.5× KDP	3.84	—	11[b]	—
26	$(NH_4)Bi_2(IO_3)_2F_5$ (ref. 48)	$P2_1$	$[BiO_2F_5]$, $[BiO_4F_4]$	9.2× KDP	3.88	0.0652@589.3 nm	6.8[b]	88.84
27	$CsVO_2F(IO_3)$ (ref. 46)	$Pna2_1$	$[VO_5F]$	1.1× KTP	2.39	0.04@2.05 μm	10.5[b]	107.9
28	$Bi_2Te(IO_3)O_5Cl$ (ref. 49)	*Cc*	$[BiO_6Cl]$	3× KDP	3.6	0.091@1.06 μm	11.1[b]	—
29	$Bi(IO_3)F_2$ (ref. 50)	*C*2	$[BiO_4F_4]$	11.5× KDP, 1× KTP	3.97	0.209@1064 nm	11[b]	—
30	$Bi_3OF_3(IO_3)_4$ (ref. 51)	$P6_3mc$	$[BiO_7F_2]$	6× KDP	3.7	0.057@532 nm	12[b]	380
31	$Sn(IO_3)_2F_2$ (ref. 52)	$P2_1$	$[SnO_4F_2]$	3× KDP	4.08	0.234@1064 nm	—	60.69
32	α-$Ba_2[VO_2F_2(IO_3)_2]IO_3$ (ref. 47)	$Pna2_1$	$[VO_4F_2]$	9× KDP	2.56	—	10.5[b]	—
33	β-$Ba_2[VO_2F_2(IO_3)_2]IO_3$ (ref. 47)	$P2_1$	$[VO_4F_2]$	9× KDP	2.89	—	10.5[b]	—
34	$CsZrF_4(IO_3)$ (ref. 53)	*Ima*2	$[ZrO_2F_6]$	4.5× KDP		0.200@1064 nm	5.8[c]	101
35	$K_5(W_3O_9F_4)(IO_3)$ (ref. 54)	*Pm*	$[WO_5F]$, $[WO_4F_2]$	11× KDP, 0.5× AGS	3.83	0.083@1064 nm	10.5[b]	200.9
36	$CdIO_3F$ (ref. 55)	$P2_12_12_1$	$[CdO_5F_2]$	6.2× KDP	4.22	0.072@1064 nm	—	—
37	KWO_3F (ref. 56)	*Ama*2	$[WO_5F]$	3× KDP	2.68	0.088@1064 nm	10[b]	129.7
38	$Pb_{17}O_8Cl_{18}$ (ref. 63)	*Fmm*2	Multiple $[PbO_2Cl_m]$	4× KDP, 2× AGS	3.44	—	13.9[c]	408

[a] The SHG intensity was measured at 1064 nm when using KDP as the reference and at ~2.1 μm when using KTP or AGS as the reference. [b] The IR cutoff edge was preliminarily measured on powder samples. [c] The IR cutoff edge was estimated on single crystals. [d] The LDT was measured on powder samples rather than single crystals.

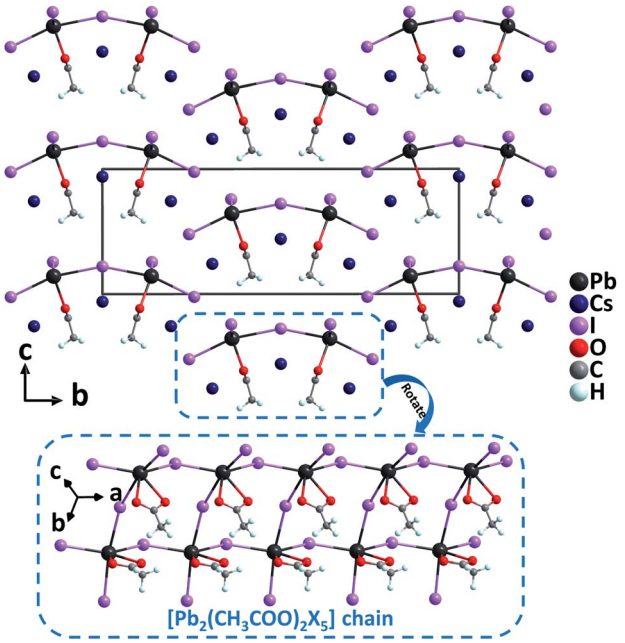

Fig. 3 Crystal structure of $Cs_3Pb_2(CH_3COO)_2I_5$ viewed along the *a*-axis (Cs–O and Cs–I bonds have been omitted for clarity).

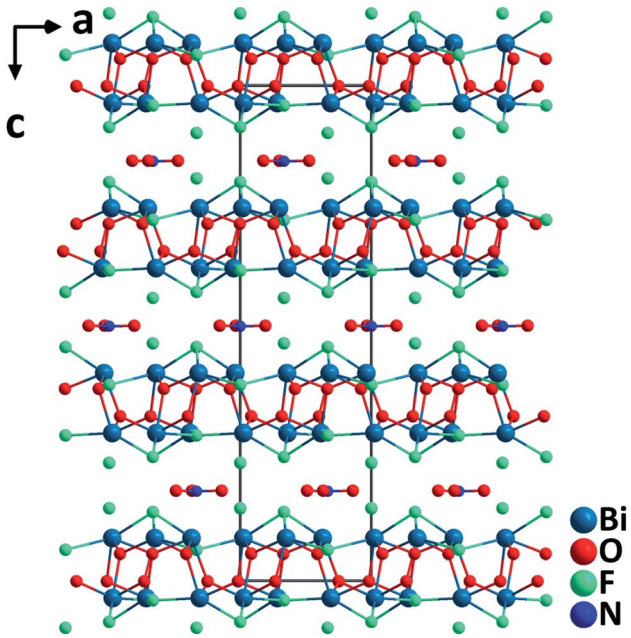

Fig. 4 Crystal structure of $Bi_6O_6F_5(NO_3)$ viewed along the *b*-axis.

group, *Cm*, and the structure is composed of corner-sharing $[CdO_2Cl_4]$ groups and $[VO_4]$ groups (Fig. 5). The Cd^{2+} cation in the $[CdO_2Cl_4]$ octahedron with a highly asymmetric coordination environment is bonded by four Cl^- and two O^{2-} with the Cd–Cl and Cd–O distances of 2.584(3)–2.859(4) Å and 2.195(6) Å, respectively. Consequently, $Cs_2CdV_2O_6Cl_2$ has a large phase-matchable SHG response of approximately 5 times that of KDP. In addition, properties of another recently reported NLO

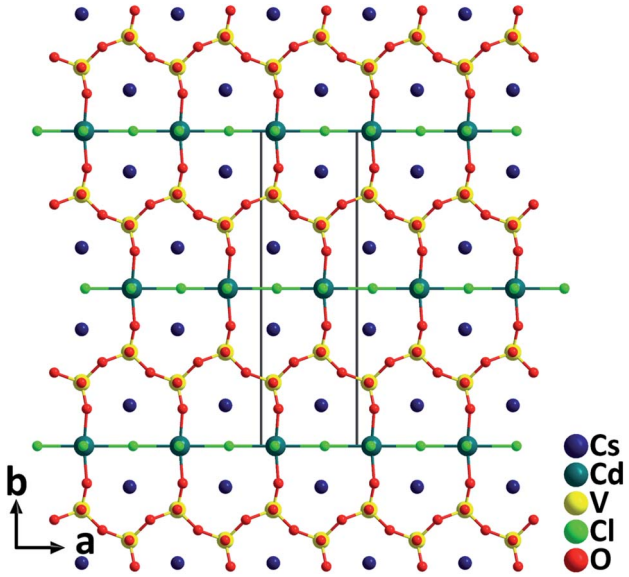

Fig. 5 Crystal structure of $Cs_2CdV_2O_6Cl_2$ viewed along the *c*-axis (Cs–O and Cs–Cl bonds have been omitted for clarity).

cadmium oxybromide vanadate, $Cs_3CdV_4O_{12}Br$[36] containing the distorted $[CdO_4Br_2]$ groups are also summarized in Table 1.

2.1.5 NLO metal oxyhalide selenites/tellurites

$BaBi(SeO_3)_2Cl$. The barium bismuth oxychloride selenite, $BaBi(SeO_3)_2Cl$ with the orthorhombic polar structure (space group: $Cmc2_1$) was synthesized through a hydrothermal reaction at a mild temperature of 200 °C.[37] The structure of $BaBi(SeO_3)_2Cl$ consists of 2D $[Bi(SeO_3)_2Cl]^{2-}$ anionic layers stacking along the [010] direction, and the charge-balancing Ba^{2+} cations are intercalated between the neighboring layers

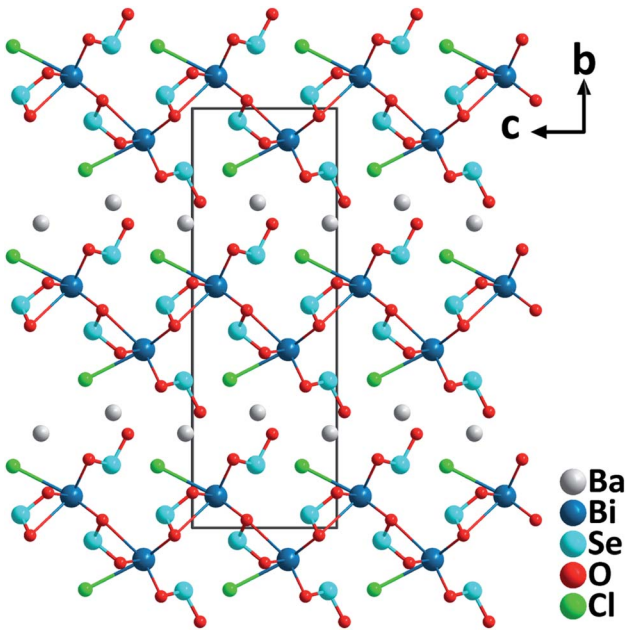

Fig. 6 Crystal structure of $BaBi(SeO_3)_2Cl$ viewed along the *a*-axis (Ba–O and Ba–Cl bonds have been omitted for clarity).

(Fig. 6). Each $[Bi(SeO_3)_2Cl]^{2-}$ layer is composed of Bi–oxychloride groups, $[BiO_8Cl]$, and $[SeO_3]$ trigonal pyramids that are bridging through oxygen atoms. Notably, the acentric $[BiO_8Cl]$ groups are aligned roughly toward the [001] direction by Cl^- ions, which is believed to generate the large macroscopic dipole moment of the compound. Excitingly, the material displays an exceptionally strong powder SHG response (16× KDP) with a phase-matching behavior at 1064 nm. In addition, the material is thermally stable up to 300 °C, has a band gap of 3.4 eV, and has a sufficient birefringence of 0.1 for phase-matching in a wide spectral range.

$BiFSeO_3$. $BiFSeO_3$ (ref. 38) was obtained by an aliovalent substitution approach using the polar model material, $BiOIO_3$ (ref. 39) with a very large SHG response (12.5× KDP). The substitution of $[SeO_3]^{2-}$ groups for $[IO_3]^-$ groups and F^- for O^{2-} has been made while the inherent structural merit of the parent compound has been maintained. As a result, $BiFSeO_3$ adopts the same NCS polar space group, $Pca2_1$, as that of $BiOIO_3$, however, it features a 3D framework rather than the layered backbone of $BiOIO_3$. The structure of $BiFSeO_3$ is constructed from 1D $[BiF]^{2+}$ chains and the bridging $[SeO_3]^{2-}$ groups through the Bi–O bonds. The seven-coordinated Bi^{3+} is bonded by five O^{2-} from five $[SeO_3]^{2-}$ anionic groups and two F^- anions, which forms a severely distorted $[BiO_5F_2]$ pentagonal bipyramid (Fig. 7). High-quality millimeter-sized $BiFSeO_3$ single crystals could be hydrothermally synthesized at 220 °C, which are stable up to 300 °C based on the TGA analysis. $BiFSeO_3$ has a larger band gap (3.83 eV) than $BiOIO_3$ (3.3 eV). Remarkably, $BiFSeO_3$ has very strong phase-matchable SHG efficiencies in both visible and NIR regions, which are about 13.5 times that of KDP at 1064 nm and 1.1 times that of KTP at 2.05 μm, respectively. Theoretical calculations indicate that the contribution percentages of $[SeO_3]$ and $[BiO_5F_2]$ to the SHG tensor, d_{31}, are 62.8% and 37.1%, respectively. Thus, the observed strong SHG response of $BiFSeO_3$ should be attributed to the synergistic effect of both $[SeO_3]$ and $[BiO_5F_2]$ NLO-active groups.

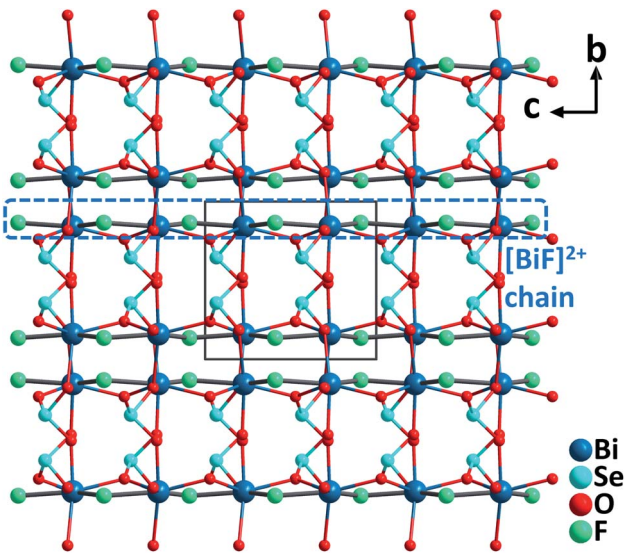

Fig. 7 Crystal structure of $BiFSeO_3$ viewed along the *a*-axis.

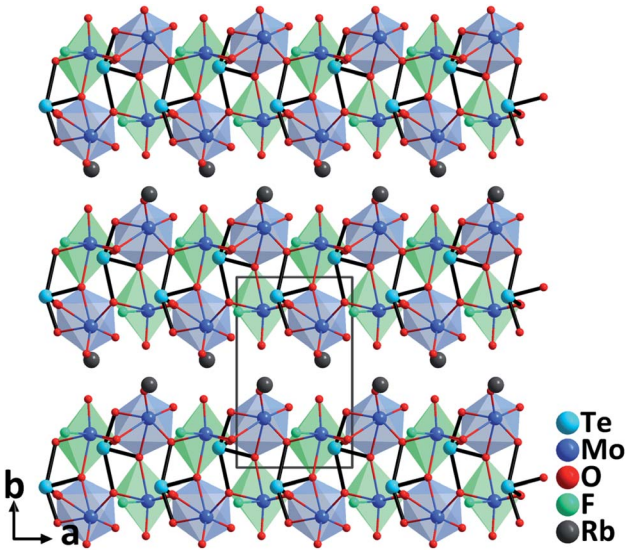

Fig. 8 Crystal structure of $RbTeMo_2O_8F$ viewed along the *c*-axis (Rb–O bonds have been omitted for clarity).

$RbTeMo_2O_8F$. Single crystals of $RbTeMo_2O_8F$ grown by a hydrothermal method at 230 °C are thermally stable up to 758 °C.[40] Belonging to the polar NCS space group, *Pn*, the structure of $RbTeMo_2O_8F$ features unique 2D $[Mo_2O_4F(TeO_4)]$ layers composed of distinctive $[MoO_5F]$ octahedra, $[MoO_6]$ octahedra, and $[TeO_4]$ units, in which both Mo^{6+} and Te^{4+} cations are in asymmetric coordination environments attributable to the SOJT effects (Fig. 8). $RbTeMo_2O_8F$ displays a layered structure similar to that of NLO $BaTeMo_2O_9$.[41] However, half of the $[MoO_6]$ groups in the $[Mo_2O_9]_\infty$ layers of $BaTeMo_2O_9$ are substituted by partially fluorinated $[MoO_5F]$ octahedra in $RbTeMo_2O_8F$, and Ba^{2+} cations residing in the interlayer space are replaced by Rb^+ to make a charge balance. More importantly, the introduction of $[MoO_5F]$ octahedra containing highly electronegative F^- not only enlarges the band gap of $RbTeMo_2O_8F$ (3.63 eV) compared to that of $BaTeMo_2O_9$ (2.95 eV), but also leads to the ordered arrangement of $[TeO_4]$ units, which in turn induces an enhanced macroscopic polarization and SHG response. The dipole moment calculations reveal that $RbTeMo_2O_8F$ exhibits a much larger net dipole moment (13.32 D) than $BaTeMo_2O_9$ (5.50 D). Besides, $RbTeMo_2O_8F$ displays the largest SHG responses (27× KDP@1064 nm, 2.2× KTP@2100 nm) among all the reported metal tellurites. The giant SHG responses can be attributed to the uniform alignment of the NLO-active units including $[MoO_5F]$, $[MoO_6]$, and $[TeO_4]$ groups with the SHG contributions of 42.2%, 25.3%, and 29.7%, respectively, based on the theoretical calculations. Moreover, the compound also has a relatively wide IR transparent window (up to 5.40 μm) and a significant birefringence (0.263@546 nm) favorable for phase-matching in NLO processes. All the attributes collectively indicate that $RbTeMo_2O_8F$ can be an outstanding candidate for Vis–NIR and mid-IR NLO materials. In addition to the above compounds, properties of other NLO metal oxyhalide selenites/tellurites such as $Cs(TiOF)_3(SeO_3)_2$,[42]

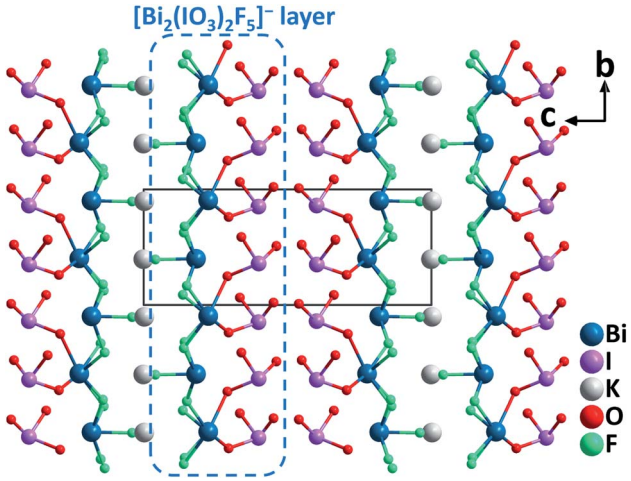

Fig. 9 Crystal structure of $KBi_2(IO_3)_2F_5$ viewed along the *a*-axis (K–F bonds have been omitted for clarity).

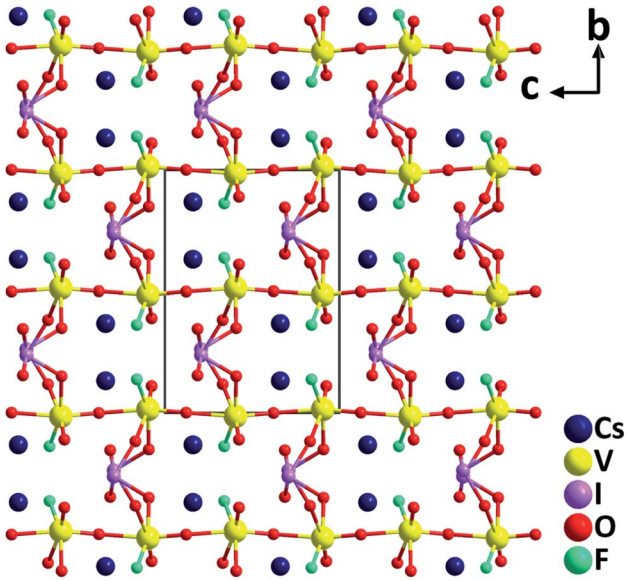

Fig. 10 Crystal structure of $CsVO_2F(IO_3)$ viewed along the *c*-axis (Cs–O and Cs–F bonds have been omitted for clarity).

$Bi_3(SeO_3)_3(Se_2O_5)F$,[43] and $Ba(MoO_2F)_2(QO_3)_2$ (Q = Se and Te)[44] are also summarized in Table 1.

2.1.6 NLO metal oxyhalide iodates

$ABi_2(IO_3)_2F_5$ (A = K, Rb, and Cs). Isostructural $ABi_2(IO_3)_2F_5$ (A = K, Rb, and Cs) were synthesized by hydrothermal reactions.[45] Crystallizing in the polar monoclinic space group, $P2_1$, their structures are characterized by 2D $[Bi_2(IO_3)_2F_5]^-$ layers formed by $[BiO_2F_4]$ oxyfluoride groups, $[BiF_5]$ groups, and $[IO_3]$ groups (Fig. 9). All the constituting units display considerable structural distortions with polar features due to the lone pair electrons on Bi^{3+} and I^{5+} cations. The well-ordered arrangement of these polar groups in $ABi_2(IO_3)_2F_5$ (A = K, Rb, and Cs) finally results in strong SHG responses of 12, 9.5, and 7.5 times that of KDP at 1064 nm. Besides, the band gaps of $ABi_2(IO_3)_2F_5$ increase slightly from K to Rb to Cs (3.75, 3.78, and 3.84 eV, respectively). TGA analyses indicate that $KBi_2(IO_3)_2F_5$ is stable up to 270 °C, while $RbBi_2(IO_3)_2F_5$ and $CsBi_2(IO_3)_2F_5$ do not show any sign of decomposition until 240 °C. Considering the remarkable SHG efficiencies with the phase-matching behavior, relatively large band gaps, and wide transparency range (0.3–11 μm), $ABi_2(IO_3)_2F_5$ could be promising candidates for mid-IR NLO applications.

$CsVO_2F(IO_3)$. The first alkali-metal vanadium oxyfluoride iodate, $CsVO_2F(IO_3)$, has been synthesized hydrothermally.[46] Crystallizing in the polar orthorhombic space group, $Pna2_1$, $CsVO_2F(IO_3)$ features a novel 3D anionic framework, $[VO_2F(IO_3)]^-$, which is composed of distorted $[VO_5F]$ octahedra and $[IO_3]$ trigonal pyramids (Fig. 10). The large magnitude of the out-of-center distortion of $[VO_5F]$ (Δ_d = 1.23) is close to that of $[VO_4F_2]$ (Δ_d = 1.20) in α-$Ba_2[VO_2F_2(IO_3)_2]IO_3$.[47] $CsVO_2F(IO_3)$ has a strong SHG response of 1.1 times that of KTP under 2.05 μm laser irradiation. Theoretical calculations reveal that the SHG contribution percentages of $[VO_5F]$, $[IO_3]$, and Cs^+ units are 62.18%, 36.05% and 1.55%, respectively. Thermal analyses indicate that the framework of the compound is stable up to 350 °C, which is relatively high for iodates. Although $CsVO_2F(IO_3)$ has a relatively small band gap (2.39 eV), the material displays a high powder LDT of 107.9 MV cm^{-2}. In addition, it has a wide IR transparent range up to 10.5 μm based on the powder measurements, suggesting its potential NLO applications in the IR region. In addition to the above compounds, characteristics of other NLO metal oxyhalide iodates such as α- and β-$Ba_2[VO_2F_2(IO_3)_2]IO_3$,[47] $(NH_4)Bi_2(IO_3)_2F_5$,[48] $Bi_2Te(IO_3)O_5Cl$,[49] $Bi(IO_3)F_2$,[50] $Bi_3OF_3(IO_3)_4$,[51] $Sn(IO_3)_2F_2$,[52] $CsZrF_4(IO_3)$,[53] $K_5(W_3O_9F_4)(IO_3)$,[54] and $CdIO_3F$[55] are also summarized in Table 1.

2.2 "Pure" metal oxyhalides with single halogen type for NLO materials

2.2.1 NLO transition metal oxyhalides

KWO_3F. Very recently, single crystals of KWO_3F were synthesized under hydrothermal conditions at 240 °C.[56] The compound crystallizes in the orthorhombic polar space group, *Ama*2. The W(VI) atom is six-coordinated by mixed ligands to form a $[WO_5F]$ distorted octahedron owing to the SOJT effect. Note that the $[WO_5F]$ octahedron has not been reported previously in other transition metal oxyhalides. While the W–O distances are 1.735–2.034 Å, that of W–F is 2.141 Å, which results in the magnitude of the out-of-center distortion (Δ_d) value of 0.65 for the $[WO_5F]$ octahedron. Each $[WO_5F]$ octahedron further polymerizes through corner-sharing with $[WO_3F]^-$ anionic layers that are stacked along the [001] direction (Fig. 11). Interestingly, the distorted octahedra are perfectly aligned in the layer, which is beneficial to produce a large SHG effect and suitable birefringence for phase-matching. Experimental results reveal that KWO_3F is thermally stable up to 350 °C in air. The compound also exhibits a large phase-matchable SHG response (3× KDP), large birefringence (0.088@1064 nm), wide IR transparent window (up to 10 μm), and relatively high powder LDT (129.7 MW cm^{-2}).

In addition, quite a few "pure" d^0/d^{10} transition metal oxyfluorides with NLO properties, such as $Sr_3Nb_2O_2F_{12}\cdot 2H_2O$,[57]

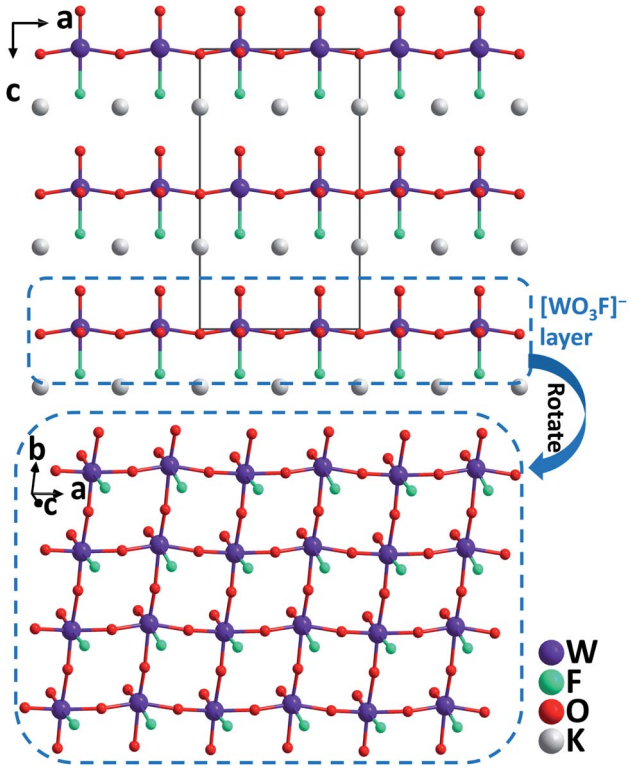

Fig. 11 Crystal structure of KWO_3F viewed along the *b*-axis (K–F and K–O bonds have been omitted for clarity).

$SrMoO_2F_4$,[58] α-$BaMoO_2F_4$,[58] $PbMoO_2F_4$,[58] $KMoO_2F_3$,[59] $NaVO_{2-x}F_{2+x}$,[60] and $KNaNbOF_5$,[61] have also been discovered recently. However, most of them exhibit relatively small SHG responses (≤1× KDP) possibly attributed to the relatively small distortions or the unfavorable arrangements of their transition metal–oxyfluoride functional units. It is worth noting that the Pan group recently performed systematic calculations and analyses of d^0 transition metal oxyfluorides with NCS structures.[62] Excitingly, they proposed that $Ba_2MoO_3F_4$ and $Ba_2WO_3F_4$ with the well-arranged anionic groups can be promising mid-IR NLO materials based on the calculations of NLO properties, in which the expected excellent properties of the materials include large NLO coefficients (corresponding to strong SHG responses, 10× KDP), wide band gaps, large IR absorption edges (10 μm), and large birefringences. This theoretical study can be an excellent guideline for the design and screening of novel mid-IR NLO materials in the transition metal oxyfluoride system.

2.2.2 NLO post-transition metal oxyhalides

$Pb_{17}O_8Cl_{18}$. The combination of heavy Pb^{2+} with possible lone pair electrons and highly electronegative Cl^- in oxides led to the discovery of a novel NLO material, $Pb_{17}O_8Cl_{18}$.[63] Remarkably, single crystals of $Pb_{17}O_8Cl_{18}$ were grown from the stoichiometric melt of PbO and $PbCl_2$ through a facile spontaneous crystallization in an open system. The size of obtained crystals is up to 7 × 2 × 2 mm^3. $Pb_{17}O_8Cl_{18}$ crystallizes in the orthorhombic polar space group, *Fmm*2, featuring a complex 3D structure composed of asymmetric $[PbO_2Cl_m]$ and $[PbCl_n]$ polyhedra. The crystal structure consists of only Pb–Cl and Pb–O bonds, which are conducive to enlarge the band gap and IR transparency, respectively, of $Pb_{17}O_8Cl_{18}$. Transmittance measurements on a single crystal reveal that $Pb_{17}O_8Cl_{18}$ has an exceptionally wide transparent range of 0.34–13.9 μm. Owing to the relatively large band gap (3.44 eV), $Pb_{17}O_8Cl_{18}$ possesses a high powder LDT, which is 12.8 times larger than that of AGS. Moreover, the material displays a very strong powder SHG effect under 2.09 μm laser irradiation, which is about 2 times larger than that of the commercial IR NLO crystal, AGS. All these attributes suggest that $Pb_{17}O_8Cl_{18}$ can be an excellent candidate for mid-IR NLO materials.

3. NLO metal oxyhalides with mixed halogen anions

3.1 $Pb_{13}O_6Cl_9Br_5$, $Pb_{13}O_6Cl_7Br_7$, and $Pb_{13}O_6Cl_4Br_{10}$

Based on the analyses that lead mixed oxyhalides could be a new promising branch for mid-IR NLO materials, systematic exploration in the PbO–$PbCl_2$–$PbBr_2$ system has been performed. The effort led to the discovery of the first examples of NLO lead mixed oxyhalides, namely, $Pb_{13}O_6Cl_9Br_5$, $Pb_{13}O_6Cl_7Br_7$, and $Pb_{13}O_6Cl_4Br_{10}$.[64] Isomorphic $Pb_{13}O_6Cl_9Br_5$, $Pb_{13}O_6Cl_7Br_7$, and $Pb_{13}O_6Cl_4Br_{10}$ all crystallize in the polar space group, *Fmm*2. Their structures are similar to that of $Pb_{17}O_8Cl_{18}$ in terms of the arrangement of oxygen-centered $[OPb_4]$ groups, which connect *via* edge-sharing and develop to parallel $[OPb_2]^{2+}$ infinite chains along the [010] direction (Fig. 12). In their structures, Pb^{2+} cations occupying the Pb(1)–Pb(7) sites are coordinated by $2O^{2-} + mCl^- + nBr^-$ anions with strongly asymmetric characteristics while those in the Pb(8) sites are coordinated exclusively by Cl^- and Br^-. Polycrystalline samples of the compounds were all synthesized by a standard solid-state reaction while the single crystals have been grown from high temperature solutions using self-fluxes of $xPbCl_2$–$yPbBr_2$. Inspiringly, large centimeter-sized (up to 2.9 × 1.3 × 0.5 cm^3) crystals of $Pb_{13}O_6Cl_9Br_5$ were successfully obtained with the aid of the top-seeded solution growth (TSSG) technique after the continuous optimization of growth parameters. Experimental results manifest that the three materials can satisfy all the fundamental criteria of high-performance mid-IR NLO materials,

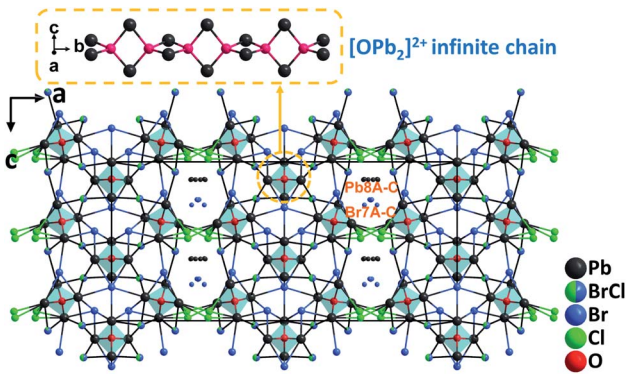

Fig. 12 Crystal structure of $Pb_{13}O_6Cl_4Br_{10}$ viewed along the *b*-axis (the coordinated bonds of Pb(8A–C) and Br(7A–C) were omitted for clarity).

including strong SHG efficiencies (0.9, 0.8, and 0.6× $AgGaS_2$@2.09 μm, respectively) with phase-matchability, wide band gaps (3.21, 3.13, and 3.05 eV, respectively), and broad IR transparency up to 14 μm. Among them, $Pb_{13}O_6Cl_9Br_5$ has shown a high LDT on a single crystal (439 MW cm^{-2}, 14.6× $AgGaS_2$) and revealed the best overall properties. This study indicates that by incorporating different types of halogen anions in one compound, the compositional diversity of lead oxyhalides can be increased compared to those with a single halogen type (F^-, Cl^-, Br^-, or I^-). It is believed that the provided feasible approach would promote the synthesis and the large crystal growth of more novel metal oxyhalides for NLO materials.

3.2 $Pb_{18}O_8Cl_{15}I_5$

Through targeted element-composition design and experience-based discovery synthesis, a novel NLO lead mixed oxyhalide, $Pb_{18}O_8Cl_{15}I_5$ was successfully obtained by our group.[65] Aiming at developing high-performance NLO materials for IR applications, the design strategy is based on the following aspects: (1) oxide-based materials have convincing advantages in crystal growth and optical properties; (2) the employment of a stereochemically active heavy metal lone pair cation, Pb^{2+}, is not only able to expand the IR transparency, but also to strengthen the SHG response; (3) the selection of a highly electronegative halide, Cl^- is conducive to enlarge the band gap and thus subsequently to achieve a high LDT; (4) by introducing the second halogen anion, I^-, which has significant differences in size and polarizability with Cl^- and O^{2-}, the coordination flexibility and diversity of Pb^{2+} can be increased. Therefore, the produced $[PbO_xCl_mI_n]$ polyhedra with a considerable distortion would be beneficialto obtain enhanced NLO properties in a material. $Pb_{18}O_8Cl_{15}I_5$ crystallizes in the monoclinic polar space group, *Cc*. As expected, Pb^{2+} cations exhibit diverse asymmetric coordination geometries and form exceptional polyhedra such as $[PbOCl_mI_n]$, $[PbO_2Cl_mI_n]$, $[PbO_3Cl_mI_n]$, and $[PbCl_mI_n]$. More interestingly, $Pb_{18}O_8Cl_{15}I_5$ not only possesses an NCS polar structure, but also exhibits the unprecedented structure featuring two different dimensional types of oxocentered Pb–O groups, *i.e.*, 0D $[O_4Pb_8]^{8+}$ clusters and 1D $[OPb_2]^{2+}$ chains (Fig. 13). Single crystals of $Pb_{18}O_8Cl_{15}I_5$ were grown by the flux method in an open system at a temperature below 400 °C. By employing the TSSG technique, centimeter-sized $Pb_{18}O_8Cl_{15}I_5$ crystals (up to 3.2 × 1.1 × 0.6 cm^3) have been successfully obtained in a short development cycle. Intriguingly, $Pb_{18}O_8Cl_{15}I_5$ displays a very strong powder phase-matching SHG response (1.05× $AgGaS_2$), applicable birefringence (0.086@636 nm), high single-crystal LDT (255 MW cm^{-2}, 8.5× $AgGaS_2$), and the widest IR transparency (up to 16.0 μm) among oxide-based materials, which are superior to those of the commercial IR NLO material, AGS. The excellent overall properties as well as the great advantage in crystal growth unambiguously demonstrate that $Pb_{18}O_8Cl_{15}I_5$ is an excellent candidate for high-performance mid-IR NLO materials. Moreover, $Pb_{18}O_8Cl_{15}I_5$ represents the first artificial metal oxyhalide with the combination of Cl^- and I^-, revealing that the structural and functional diversity of metal oxyhalides can be greatly increased through the incorporation of different kinds of halogen anions.

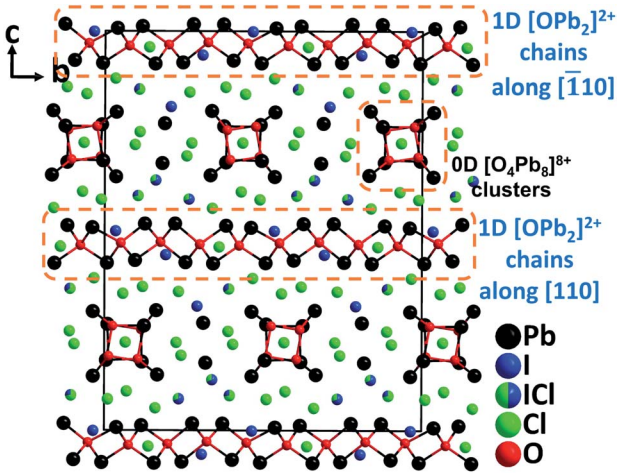

Fig. 13 Crystal structure of $Pb_{18}O_8Cl_{15}I_5$ viewed along the *a*-axis (Pb–Cl and Pb–I bonds have been omitted for clarity).

3.3 $CsZn_2BO_3FCl$

Single crystals of $CsZn_2BO_3FCl$ were synthesized *via* the high temperature solution method.[32] Crystallizing in the polar space group, *R*3, $CsZn_2BO_3FCl$ contains $[Zn_2BO_3FCl]$ layers that resemble the $[Be_2BO_3F_2]$ layers in KBBF (Fig. 14). Note that $CsZn_2BO_3FCl$ is the first example in the KBBF family with mixed halogen anions. In the structure, F and Cl occupy different individual crystallographic sites; thus, [Zn(1)O_3F] and [Zn(2)O_3Cl] tetrahedra are formed, respectively, in $CsZn_2BO_3FCl$. Interestingly, two other compounds with single type halogen anions, isostructural $CsZn_2BO_3F_2$ and $CsZn_2BO_3Cl_2$ crystallize in the nonpolar NCS space group, *R*32. $CsZn_2BO_3FCl$ reveals more enhanced SHG responses (3.5× KDP@1064 nm, 0.58× BBO@532 nm) compared to those of $CsZn_2BO_3F_2$ (3.2× KDP@1064 nm, 0.54× BBO@532 nm) and $CsZn_2BO_3Cl_2$ (2.8× KDP@1064 nm, 0.50× BBO@532 nm), which is probably induced by the mixed halogen anions, F^- and Cl^- with a large electronegativity difference in $CsZn_2BO_3FCl$. Theoretical real-space atom-cutting analyses of the SHG effect reveal that the contributions of $[ZnO_3X]$ (X = F and Cl) and $[BO_3]$ are comparable while Cs^+ makes little contribution. Thermal analyses indicate that the compound melts incongruently and is stable up to 677 °C. Moreover, the compound has a very short UV cutoff edge (<190 nm), indicating that $CsZn_2BO_3FCl$ could be a potential UV and DUV NLO material.

3.4 $Cs_3Pb_2(CH_3COO)_2Br_3I_2$

By the partial substitution of Br^- anions in $Cs_3Pb_2(CH_3COO)_2Br_5$ for I^-, a new isostructural compound, $Cs_3Pb_2(CH_3COO)_2Br_3I_2$, has been obtained under mixed-solvothermal conditions.[66] Different from $Cs_3Pb_2(CH_3COO)_2Br_5$ with single halogen type, the structure of $Cs_3Pb_2(CH_3COO)_2Br_3I_2$ contains

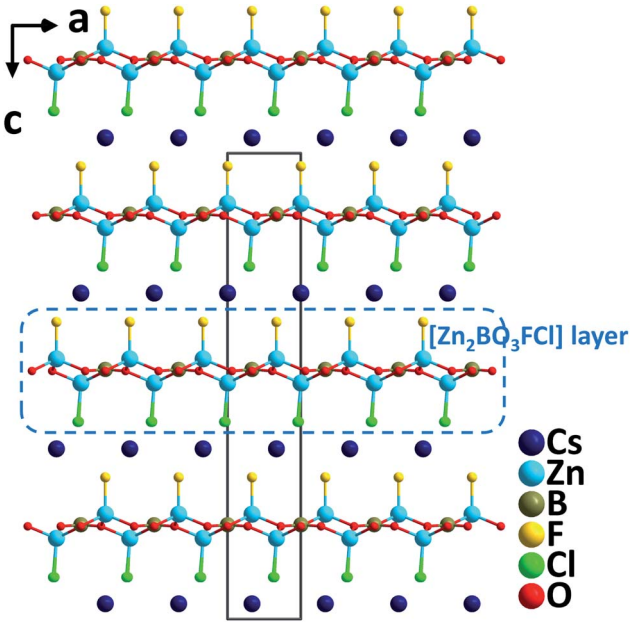

Fig. 14 Crystal structure of $CsZn_2BO_3FCl$ projected along the *b*-axis (Cs–Cl and Cs–F bonds have been omitted for clarity).

rare Pb–mixed-oxyhalide polyhedra, $[PbO_2Br_2I_2]$ (Fig. 15), which are severely distorted and exhibit a larger polarizability. Consequently, the compound displays an enhanced SHG response (9× KDP) and enlarged birefringence (0.27@1064 nm) compared to $Cs_3Pb_2(CH_3COO)_2Br_5$ (4× KDP, 0.15@1064 nm) and $Cs_3Pb_2(CH_3COO)_2I_5$ (8× KDP, 0.26@1064 nm). The results manifest that the well-arranged $PbBr_2I_2O_2$ polyhedra composed of Pb^{2+} with the stereochemically active lone pair and multiple types of anions (O^{2-}, Br^-, and I^-) with different ionic radius, electronegativity, and coordination capability, can not only enhance the polarizability to strengthen the SHG response, but also improve the anisotropy to enlarge the birefringence of a material.

3.5 $Pb_2TiOF(SeO_3)_2Cl$ and its analogs

$Pb_2TiOF(SeO_3)_2Cl$ was discovered by a hydrothermal synthesis during the efforts of introducing the halogen anions into the Pb-d^0 transition metal–selenite system.[67] The compound crystallizes in the polar monoclinic space group, $P2_1$, exhibiting

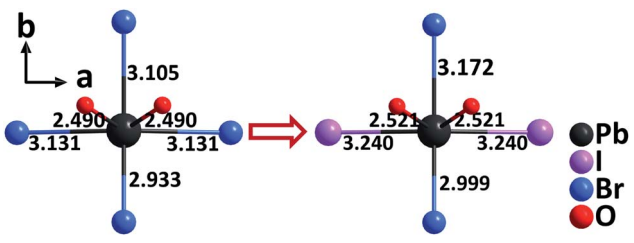

Fig. 15 The evolution from the $[PbO_2Br_4]$ polyhedron to the $[PbBr_2I_2O_2]$ polyhedron by the substitution of two Br^- anions for two I^- anions.

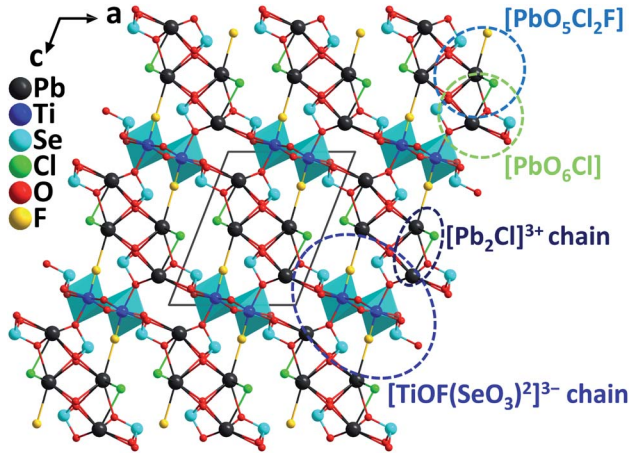

Fig. 16 Crystal structure of $Pb_2TiOF(SeO_3)_2Cl$ viewed along the *b*-axis.

a novel 3D network constructed from 1D $[ClPb_2]^{3+}$ cationic chains and 1D $[TiOF(SeO_3)^2]^{3-}$ anionic chains that are composed of Ti^{4+}–oxyfluoride group, $[TiO_5F]$ distorted octahedra, and $[SeO_3]$ groups (Fig. 16). The calculated magnitude of the out-of-center distortion (Δ_d) is 0.6183. The Pb atoms in $Pb_2TiOF(SeO_3)_2Cl$ have two kinds of coordination environment, producing Pb–oxychloride $[PbO_6Cl]$ polyhedra and Pb–mixed-oxyhalide $[PbO_5Cl_2F]$ polyhedra, which are all severely distorted due to the presence of the lone pair electrons on Pb^{2+}. Powder SHG tests reveal that $Pb_2TiOF(SeO_3)_2Cl$ has strong phase-matchable SHG responses of 9.6 times that of KDP at 1064 nm and 0.65 times that of KTP at 2050 nm. The collaborative polarizations from the asymmetric NLO-active units, including $[PbO_5Cl_2F]$, $[PbO_6Cl]$, $[TiO_5F]$, and $[SeO_3]$, should be responsible for the large SHG effect in $Pb_2TiOF(SeO_3)_2Cl$. It is interesting to note that another isostructural compound, $Pb_2NbO_2(SeO_3)_2Cl$, displays a much weaker SHG response (2.3× KDP).[67] For $Pb_2NbO_2(SeO_3)_2Cl$, the main structural differences are the replacement of $[TiO_5F]$, $[PbO_5Cl_2F]$, and $[PbO_6Cl]$ with $[NbO_6]$, $[PbO_6Cl_2]$, and $[PbO_5Cl]$. Therefore, the introduction of a second type halogen anion, F^-, is likely to induce a stronger SHG response, which has been subsequently demonstrated by analyzing the band structures of the two compounds based on the first-principles calculations. Remarkably, Liu *et al.* have successfully synthesized the bromide analog, $Pb_2TiFO(SeO_3)_2Br$[68] with a larger SHG response (10× KDP), which is probably more difficult to obtain in the synthesis due to the increased difference between Br^- and F^-. Similar to the coordination in $Pb_2TiFO(SeO_3)_2Cl$, $[TiO_5F]$, $[PbO_6Br]$, and $[PbO_5Br_2F]$ polyhedra are observed in $Pb_2TiFO(SeO_3)_2Br$, however, we noticed that the Pb–mixed-oxyhalide unit, $[PbO_5Br_2F]$, combining F^- and Br^- is quite rare, except for the case in another analog, $Pb_2GaF_2(SeO_3)_2Br$, which displays an SHG response which is 4.5 times that of KDP.[69] In addition, through the band engineering strategy achieved by the aliovalent substitution, isomorphic $Pb_2GaF_2(SeO_3)_2Cl$ has also been obtained, which exhibits the widest band gap (4.32 eV) among all the reported phase-matchable NLO selenites while maintaining a relatively large SHG response (4.5× KDP).[70]

4. Conclusions and outlook

In summary, the recent significant advancements of NLO metal oxyhalides have been reviewed. Forty eight NLO metal oxyhalides with various metal–oxyhalide functional units have been presented in Tables 1 and 2. Compared to the traditional metal–oxide functional units, metal–oxyhalide units combining O^{2-} and X^- (X = F, Cl, Br, and I) clearly result in diverse metal-centered polyhedra with considerable distortions, especially when more than one type of X^- is incorporated. These distorted metal–oxyhalide polyhedra can serve as both NLO-active units and birefringence-active units, which have been demonstrated to be helpful in realizing strong SHG responses and large birefringences in NLO materials. Besides, the band gaps, SHG responses, and even other properties of metal oxyhalides can be possibly tuned based on the same or similar structural configurations by choosing different halogen anions, as can be seen in $Pb_2B_5O_9X$ (X = Cl, Br, and I), $Cs_3Pb_2(CH_3COO)_2X_5$ (X = Br and I), $Cs_3Pb_2(CH_3COO)_2Br_3I_2$, $Pb_{13}O_6Cl_9Br_5$, $Pb_{13}O_6Cl_7Br_7$, and $Pb_{13}O_6Cl_4Br_{10}$. It is worth noting that the participation of additional types of metal cations, for example, alkali metal cations in $ABi_2(IO_3)_2F_5$ (A = K, Rb, and Cs), $Rb_3Pb_2(CH_3COO)_2X_5$ (X = Br and Cl), and $CsVO_2F(IO_3)$, alkaline-earth metal cation, Ba^{2+} in $BaBi(SeO_3)_2Cl$, could be a useful way to regulate the arrangement of functional groups and the structural configuration, although these additional metal cations may make little direct contributions to the NLO properties. More broadly, this method is also applicable to "pure" metal oxyhalides with a single type halogen anion and metal oxyhalides with mixed halogen anions.

It is found that for the classic metal oxyhalides with a single halogen type, incorporating additional NLO-active anionic groups ($[BO_3]$, $[BO_4]$, $[CH_3COO]$, $[NO_3]$, $[VO_6]$, $[SeO_3]$, $[IO_3]$, *etc.*), is a very effective way to design and synthesize NLO metal oxyhalide compounds exhibiting strong SHG responses. The strong SHG responses usually originate from the synergistic effects of distorted metal–oxyhalide groups and the additional anionic groups. Further structure–NLO property relationship analyses revealed that enhanced SHG effects can be achieved (*e.g.*, 27× KDP for $RbTeMo_2O_8F$, 16× KDP for $BaBi(SeO_3)_2Cl$, 13.5× KDP for $Pb_2B_5O_9I$, 12.5× KDP for $BiFSeO_3$, and 12× KDP for $ABi_2(IO_3)_2F_5$) when all the NLO-active groups are well-aligned. However, the SHG responses would be hindered if the NLO-active groups are arranged irregularly or in an antiparallel manner. From the viewpoint of structural chemistry, the introduction of additional anionic groups to metal oxyhalides can not only tremendously enrich the diversity of crystal structures, but also be conducive to the arrangement of all the functional groups. This can be proved by comparing the metal oxyhalides containing additional anionic groups with "pure" single-halogen metal oxyhalides, in which the metal–oxyhalide groups are usually more difficult to be well-aligned. Moreover, the increased structural tunability of single-halogen metal oxyhalides with additional anionic groups makes it more achievable to tune the overall NLO-related properties guided by anionic group theory, band engineering strategy, and rational composition design. From the cases of metal oxyhalides with

Table 2 Space groups, metal–oxyhalide unit types, and key properties of NLO metal oxyhalides with mixed halogen anions

No.	Crystal	Space group	Metal–oxyhalide unit type	SHG[a]	E_g (eV)	Birefringence	IR cutoff edge (μm)	LDT (MW cm^{-2})
1	$Pb_{13}O_6Cl_9Br_5$ (ref. 64)	*Fmm*2	Multiple $[PbO_2Cl_mBr_n]$	0.9× AGS	3.23	—	14.0[c]	439[e]
2	$Pb_{13}O_6Cl_7Br_7$ (ref. 64)	*Fmm*2	Multiple $[PbO_2Cl_mBr_n]$	0.8× AGS	3.13	—	6.0[b]	—
3	$Pb_{13}O_6Cl_4Br_{10}$ (ref. 64)	*Fmm*2	Multiple $[PbO_2Cl_mBr_n]$	0.6× AGS	3.05	—	6.0[b]	—
4	$Pb_{18}O_8Cl_{15}I_5$ (ref. 65)	*Cc*	Multiple $[PbOCl_mI_n]$, $[PbO_2Cl_mI_n]$, $[PbO_3Cl_mI_n]$	1.05× AGS	2.82	0.086@636 nm (exp.)	16.0[c]	255[e]
5	$CsZn_2BO_3FCl$ (ref. 32)	*R*3	$[ZnO_3F]$, $[ZnO_3Cl]$	3.5× KDP	>6.5	—	—	—
6	$Cs_3Pb_2(CH_3COO)_2Br_3I_2$ (ref. 66)	*Amm*2	$[PbO_2Br_2I_2]$	9× KDP	2.70	0.27@1064 nm (calc.)	6.0[b]	39[d]
7	$Pb_2TiOF(SeO_3)_2Cl$ (ref. 67)	$P2_1$	$[PbO_3Cl_2F]$, $[PbO_6Cl]$, $[TiO_5F]$	9.6× KDP, 0.65× KTP	3.34	—	—	—
8	$Pb_2TiFO(SeO_3)_2Br$ (ref. 68)	$P2_1$	$[PbO_3Br_2F]$, $[PbO_6Br]$, $[TiO_5F]$	10× KDP	3.26	0.19@1064 nm (calc.)	10[b]	—
9	$Pb_2GaF_2(SeO_3)_2Br$ (ref. 69)	$P2_1$	$[PbO_3Br_2F]$, $[PbO_6Br]$, $[GaO_3F_3]$	4.5× KDP	3.73	—	—	—
10	$Pb_2GaF_2(SeO_3)_2Cl$ (ref. 70)	$P2_1$	$[PbO_3Cl_2F]$, $[PbO_6Cl]$, $[GaO_3F_3]$	4.5× KDP	4.32	—	11[b]	120[d]

[a] The SHG intensity was measured at 1064 nm when using KDP as the reference and at ~2.1 μm when using KTP or AGS as the reference. [b] The IR cutoff edge was preliminarily measured on powder samples. [c] The IR cutoff edge was estimated on single crystals. [d] The LDT was preliminarily measured on powder samples. [e] The LDT was estimated on single crystals.

mixed halogen anions, it is found that the targeted combination of different halogen anions in one compound has become a feasible and compelling way to produce more NLO metal oxyhalides with increased compositional and structural diversification. However, the development of NLO metal oxyhalides with mixed halogen anions is still in the primary stage.

In terms of the application prospects, NLO metal oxyhalides with additional anionic groups can be promising candidates for NLO materials working in the Vis–NIR region and mid-IR region of the 3–5 μm atmospheric window if their large single crystals can be successfully grown in the future. However, the combination of various anionic groups in one compound usually increases the difficulty in large single crystal growth. For mid-IR NLO materials working beyond 5 μm, a more careful chemical composition design should be taken into consideration because the introduction of relatively light atoms needs to be avoided in order to achieve a wider IR transparency. In this aspect, the emerging heavy metal mixed oxyhalides without traditional metal–oxide anionic groups, for example, $Pb_{18}O_8Cl_{15}I_5$ and $Pb_{13}O_6Cl_9Br_5$, have manifested unprecedented advantages in both structural diversity and functionality compared to other oxide-based compounds for mid-IR NLO materials. More inspiringly, centimeter-sized single crystals of $Pb_{18}O_8Cl_{15}I_5$ and $Pb_{13}O_6Cl_9Br_5$ have been successfully grown by a feasible method in a relatively short development cycle. Therefore, considering the excellent potential in structural diversity and tunability as well as the consequently fascinating overall properties, we firmly believe that more novel metal oxyhalides with additional anionic groups and metal oxyhalides with mixed halogen anions will be discovered, and this emerging branch can provide very competitive candidates for high-performance NLO materials, especially in Vis–NIR and mid-IR regions.

Author contributions

Both authors contributed to the conceptualization, writing, and editing of the manuscript.

Conflicts of interest

There are no conflicts to declare.

Acknowledgements

This work was supported by the National Research Foundation of Korea (NRF) funded by the Ministry of Science and ICT (Grant No. 2018R1A5A1025208 and 2019R1A2C3005530).

Notes and references

1 (*a*) P. A. Franken, A. E. Hill, C. W. Peters and G. Weinreich, *Phys. Rev. Lett.*, 1961, **7**, 118–119; (*b*) D. A. Keszler, *Curr. Opin. Solid State Mater. Sci.*, 1996, **1**, 204–208.

2 (*a*) D. Cyranoski, *Nature*, 2009, **457**, 953–955; (*b*) D. N. Nikogosyan, *Nonlinear optical crystals: A complete survey*, Springer Science, New York, 2005; (*c*) C. T. Chen, T. Sasaki, R. K. Li, Y. C. Wu, Z. S. Lin and Y. Mori, *Nonlinear optical borate crystals: Principals and applications*, John Wiley & Sons, 2012.

3 (*a*) P. S. Halasyamani and K. R. Poeppelmeier, *Chem. Mater.*, 1998, **10**, 2753–2769; (*b*) N. Savage, *Nat. Photonics*, 2007, **1**, 83–85; (*c*) C. T. Chen, Y. B. Wang, B. C. Wu, K. C. Wu, W. L. Zeng and L. H. Yu, *Nature*, 1995, **373**, 322–324.

4 A. O. Okorogu, S. B. Mirov, W. Lee, D. I. Crouthamel, N. Jenkins, A. Y. Dergachev, K. L. Vodopyanov and V. V. Badikov, *Opt. Commun.*, 1998, **155**, 307–312.

5 G. D. Boyd, F. G. Storz, J. H. McFee and H. M. Kasper, *IEEE J. Quantum Electron.*, 1972, **8**, 900–908.

6 G. D. Boyd, *Appl. Phys. Lett.*, 1971, **18**, 301–304.

7 J. D. Bierlein and H. Vanherzeele, *J. Opt. Soc. Am. B*, 1989, **6**, 622–633.

8 G. D. Boyd, R. C. Miller, K. Nassau, W. L. Bond and A. Savage, *Appl. Phys. Lett.*, 1964, **5**, 234–236.

9 W. L. Smith, *Appl. Opt.*, 1977, **16**, 1798–8.

10 C. T. Chen, B. C. Wu, A. D. Jiang and G. M. You, *Sci. China, Ser. B: Chem., Life Sci., Earth Sci.*, 1985, **28**, 235–243.

11 C. T. Chen, Y. C. Wu, A. D. Jiang, B. C. Wu, G. M. You, R. K. Li and S. J. Lin, *J. Opt. Soc. Am. B*, 1989, **6**, 616–621.

12 Y. Mori, I. Kuroda, S. Nakajima, T. Sasaki and S. Nakai, *Appl. Phys. Lett.*, 1995, **67**, 1818–1820.

13 C. T. Chen, G. L. Wang, X. Y. Wang and Z. Y. Xu, *Appl. Phys. B: Lasers Opt.*, 2009, **97**, 9–25.

14 (*a*) K. Wu and S. Pan, *Coord. Chem. Rev.*, 2018, **377**, 191–208; (*b*) V. G. Dmitriev, G. G. Gurzadyan and D. N. Nikogosyan, *Handbook of Nonlinear Optical Crystals*, 3rd edn, Springer, Heidelberg, 1999.

15 (*a*) Z.-G. Hu, M. Yoshimura, Y. Mori and T. Sasaki, *J. Cryst. Growth*, 2005, **275**, 232–239; (*b*) C. T. Chen, L. Bai, Z. Z. Wang and R. K. Li, *J. Cryst. Growth*, 2006, **292**, 169–178.

16 W. Zhang, H. Yu, H. Wu and P. S. Halasyamani, *Chem. Mater.*, 2017, **29**, 2655–2668.

17 (*a*) A. G. Jackson, M. C. Ohmer and S. R. LeClair, *Infrared Phys. Technol.*, 1997, **38**, 233–244; (*b*) F. Liang, L. Kang, Z. Lin and Y. Wu, *Cryst. Growth Des.*, 2017, **17**, 2254–2289; (*c*) X. Luo, Z. Li, Y. Guo, J. Yao and Y. Wu, *J. Solid State Chem.*, 2019, **270**, 674–687.

18 (*a*) J. Lu, Y.-K. Lian, L. Xiong, Q.-R. Wu, M. Zhao, K.-X. Shi, L. Chen and L.-M. Wu, *J. Am. Chem. Soc.*, 2019, **141**, 16151–16159; (*b*) Z. Xia and K. R. Poeppelmeier, *Acc. Chem. Res.*, 2017, **50**, 1222–1230; (*c*) K. M. Ok, *Acc. Chem. Res.*, 2016, **49**, 2774–2785; (*d*) Y. Wang and S. Pan, *Coord. Chem. Rev.*, 2016, **323**, 15–35; (*e*) M. Mutailipu, K. R. Poeppelmeier and S. Pan, *Chem. Rev.*, 2021, **121**, 1130–1202; (*f*) Y. Pan, S.-P. Guo, B.-W. Liu, H.-G. Xue and G.-C. Guo, *Coord. Chem. Rev.*, 2018, **374**, 464–496.

19 (*a*) Y.-Y. Li, P.-F. Liu and L.-M. Wu, *Chem. Mater.*, 2017, **29**, 5259–5266; (*b*) H.-M. Zhou, L. Xiong, L. Chen and L.-M. Wu, *Angew. Chem., Int. Ed.*, 2019, **58**, 9979–9983; (*c*) F. Liang, L. Kang, Z. Lin, Y. Wu and C. Chen, *Coord. Chem. Rev.*, 2017, **333**, 57–70; (*d*) S.-P. Guo, X. Cheng, Z.-D. Sun, Y. Chi, B.-W. Liu, X.-M. Jiang, S.-F. Li, H.-G. Xue, S. Deng, V. Duppel, J. Khler and G.-C. Guo, *Angew. Chem., Int. Ed.*, 2019, **58**, 8087–8091; (*e*) G. Li, Y. Chu and Z. Zhou, *Chem. Mater.*, 2018, **30**, 602–606; (*f*) G. Li, K. Wu, Q. Liu, Z. Yang

and S. Pan, *J. Am. Chem. Soc.*, 2016, **138**, 7422–7428; (*g*) Y. Guo, F. Liang, W. Yin, Z. Li, X. Luo, Z. S. Lin, J. Yao, A. Mar and Y. Wu, *Chem. Mater.*, 2019, **31**, 3034–3040.

20 (*a*) P. Gong, F. Liang, L. Kang, X. Chen, J. Qin, Y. Wu and Z. Lin, *Coord. Chem. Rev.*, 2019, **380**, 83–102; (*b*) Y. Huang, X. Meng, P. Gong, Z. Lin, X. Chen and J. Qin, *J. Mater. Chem. C*, 2015, **3**, 9588–9593; (*c*) Q. Wu, X. Meng, C. Zhong, X. Chen and J. Qin, *J. Am. Chem. Soc.*, 2014, **136**, 5683–5686; (*d*) G. Zhang, Y. Li, K. Jiang, H. Zeng, T. Liu, X. Chen, J. Qin, Z. Lin, P. Fu, Y. Wu and C. Chen, *J. Am. Chem. Soc.*, 2012, **134**, 14818–14822; (*e*) Y. Li, M. Wang, T. Zhu, X. Meng, C. Zhong, X. Chen and J. Qin, *Dalton Trans.*, 2012, **41**, 763–766; (*f*) G. Zhang, J. Qin, T. Liu, Y. Li, Y. Wu and C. Chen, *Appl. Phys. Lett.*, 2009, **95**, 261104; (*g*) T. Liu, J. Qin, G. Zhang, T. Zhu, F. Niu, Y. Wu and C. Chen, *Appl. Phys. Lett.*, 2008, **93**, 091102.

21 (*a*) D. Lin, M. Luo, C. Lin, F. Xu and N. Ye, *J. Am. Chem. Soc.*, 2019, **141**, 3390–3394; (*b*) M. Xia, X. Jiang, Z. Lin and R. Li, *J. Am. Chem. Soc.*, 2016, **138**, 14190–14193; (*c*) X. Chen, F. Zhang, L. Liu, B. H. Lei, X. Dong, Z. Yang, H. Li and S. Pan, *Phys. Chem. Chem. Phys.*, 2016, **18**, 4362–4369; (*d*) L. Y. Li, G. B. Li, Y. X. Wang, F. H. Liao and J. H. Lin, *Chem. Mater.*, 2005, **17**, 4174–4180; (*e*) P. Becker, *Adv. Mater.*, 1998, **10**, 979–992; (*f*) H. Lee and K. M. Ok, *Bull. Korean Chem. Soc.*, 2020, **41**, 139–142.

22 (*a*) G. Han, Y. Wang, B. Zhang and S. Pan, *Chem.–Eur. J.*, 2018, **24**, 17638–17650; (*b*) M. Mutailipu, M. Zhang, Z. Yang and S. Pan, *Acc. Chem. Res.*, 2019, **52**, 791–801; (*c*) G. Shi, Y. Wang, F. Zhang, B. Zhang, Z. Yang, X. Hou, S. Pan and K. R. Poeppelmeier, *J. Am. Chem. Soc.*, 2017, **139**, 10645–10648; (*d*) M. Luo, F. Liang, Y. Song, D. Zhao, F. Xu, N. Ye and Z. Lin, *J. Am. Chem. Soc.*, 2018, **140**, 3884–3887; (*e*) M. Mutailipu and S. Pan, *Angew. Chem., Int. Ed.*, 2020, **59**, 20302–20317.

23 (*a*) J. Lu, J.-N. Yue, L. Xiong, W.-K. Zhang, L. Chen and L.-M. Wu, *J. Am. Chem. Soc.*, 2019, **141**, 8093–8097; (*b*) B. Zhang, G. Han, Y. Wang, X. Chen, Z. Yang and S. Pan, *Chem. Mater.*, 2018, **30**, 5397–5403; (*c*) L. Xiong, J. Chen, J. Lu, C.-Y. Pan and L.-M. Wu, *Chem. Mater.*, 2018, **30**, 7823–7830; (*d*) G. Han, B.-H. Lei, Z. Yang, Y. Wang and S. Pan, *Angew. Chem., Int. Ed.*, 2018, **57**, 9828–9832.

24 (*a*) Z. H. Yang, C. Hu, M. Mutailipu, Y. Z. Sun, K. Wu, M. Zhang and S. L. Pan, *J. Mater. Chem. C*, 2018, **6**, 2435–2442; (*b*) X. Dong, L. Huang, C. Hu, H. Zeng, Z. Lin, X. Wang, K. M. Ok and G. Zou, *Angew. Chem., Int. Ed.*, 2019, **58**, 6528–6534; (*c*) Y. Deng, L. Huang, X. Dong, L. Wang, K. M. Ok, H. Zeng, Z. Lin and G. Zou, *Angew. Chem., Int. Ed.*, 2020, **59**, 21151–21156; (*d*) L. Wang, F. Yang, X. Zhao, L. Huang, D. Gao, J. Bi, X. Wang and G. Zou, *Dalton Trans.*, 2019, **48**, 15144–15150; (*e*) L. Liu, L. Wang, R. Guo, Z. Hou, Z. Fang and X. Wang, *J. Cryst. Growth*, 2020, **542**, 125689.

25 (*a*) B.-W. Liu, H.-Y. Zeng, X.-M. Jiang, G.-E. Wang, S.-F. Li, L. Xu and G.-C. Guo, *Chem. Sci.*, 2016, **7**, 6273–6277; (*b*) B.-W. Liu, X.-M. Jiang, B.-X. Li, H.-Y. Zeng and G.-C. Guo, *Angew. Chem., Int. Ed.*, 2020, **132**, 4886–4889; (*c*) B.-W. Liu, H.-Y. Zeng, X.-M. Jiang and G.-C. Guo, *CCS Chem.*, 2020, **2**, 964–973; (*d*) B.-W. Liu, X.-M. Jiang, H.-Y. Zeng and G.-C. Guo, *J. Am. Chem. Soc.*, 2020, **142**, 10641–10645; (*e*) R. Wang, X. Zhang, J. He, K. Bu, C. Zheng, J. Lin and F. Huang, *Inorg. Chem.*, 2018, **57**, 1449–1454; (*f*) L. Gao, J. Huang, S. Guo, Z. Yang and S. Pan, *Coord. Chem. Rev.*, 2020, **421**, 213379.

26 (*a*) H. Yan, Y. Matsushita, K. Yamaura and Y. Tsujimoto, *Angew. Chem., Int. Ed.*, 2021, **60**, 26561–26565; (*b*) R. Wang, F. Liang, F. Wang, Y. Guo, X. Zhang, Y. Xiao, K. Bu, Z. Lin, J. Yao, T. Zhai and F. Huang, *Angew. Chem., Int. Ed.*, 2019, **58**, 8078–8081; (*c*) Y. Tsujimoto, C. A. Juillerat, W. Zhang, K. Fujii, M. Yashima, P. S. Halasyamani and H. C. zur Loye, *Chem. Mater.*, 2018, **30**, 6486–6493; (*d*) B.-W. Liu, X.-M. Jiang, G.-E. Wang, H.-Y. Zeng, M.-J. Zhang, S.-F. Li, W.-H. Guo and G. C. Guo, *Chem. Mater.*, 2015, **27**, 8189–8192; (*e*) A. Reshak, *Sci. Rep.*, 2017, **7**, 46415; (*f*) N. J. Takas and J. A. Aitken, *Inorg. Chem.*, 2006, **45**, 2779–2781; (*g*) T. Sambrook, C. F. Smura, S. J. Clarke, K. M. Ok and P. S. Halasyamani, *Inorg. Chem.*, 2007, **46**, 2571–2574.

27 (*a*) U. Opik and M. H. L. Pryce, *Proc. R. Soc. London, Ser. A*, 1957, **238**, 425–447; (*b*) R. G. Pearson, *J. Am. Chem. Soc.*, 1969, **91**, 4947–4955; (*c*) R. A. Wheeler, M.-H. Whangbo, T. Hughbanks, R. Hoffmann, J. K. Burdett and T. A. Albright, *J. Am. Chem. Soc.*, 1986, **108**, 2222–2236; (*d*) J. Y. Hwang and K. M. Ok, *Bull. Korean Chem. Soc.*, 2020, **41**, 588–591.

28 G. Zou, C. Lin, H. Jo, G. Nam, T. S. You and K. M. Ok, *Angew. Chem., Int. Ed.*, 2016, **55**, 12078–12082.

29 M. Luo, Y. Song, F. Liang, N. Ye and Z. Lin, *Inorg. Chem. Front.*, 2018, **5**, 916–921.

30 H. Yu, N. Z. Koocher, J. M. Rondinelli and P. S. Halasyamani, *Angew. Chem., Int. Ed.*, 2018, **57**, 6100–6103.

31 (*a*) Y.-Z. Huang, L.-M. Wu, X.-T. Wu, L.-H. Li, L. Chen and Y.-F. Zhang, *J. Am. Chem. Soc.*, 2010, **132**, 12788–12789; (*b*) P. A. Plachinda, V. A. Dolgikh, S. Y. Stefanovich and P. S. Berdonosov, *Solid State Sci.*, 2005, **7**, 1194–1200; (*c*) B. V. Egorova, A. V. Olenev, P. S. Berdonosov, A. N. Kuznetsov, S. Y. Stefanovich, V. A. Dolgikh, T. Mahenthirarajah and P. Lightfoot, *J. Solid State Chem.*, 2008, **181**, 1891–1898; (*d*) Z. Chen, S. Pan, Z. Yang, X. Dong, X. Su and Y. Yang, *J. Mater. Sci.*, 2013, **48**, 2590–2596.

32 J. Zhou, Y. Liu, H. Wu, H. Yu, Z. Lin, Z. Hu, J. Wang and Y. Wu, *Angew. Chem., Int. Ed.*, 2020, **59**, 19006–19010.

33 Q.-R. Shui, H.-X. Tang, R.-B. Fu, Y.-B. Fang, Z.-J. Ma and X.-T. Wu, *Angew. Chem., Int. Ed.*, 2017, **60**, 2116–2119.

34 Q. Shui, R. Fu, H. Tang, Y. Fang, Z. Ma and X. Wu, *Inorg. Chem.*, 2021, **60**, 5290–5296.

35 E. J. Cho, S.-J. Oh, H. Jo, J. Lee, T.-S. You and K. M. Ok, *Inorg. Chem.*, 2019, **58**, 2183–2190.

36 Y. Li, D. Zhang, L. Liu, W. Zhang, J. Zhang, Y. Cong, X. Li and P. S. Halasyamani, *Dalton Trans.*, 2019, **48**, 10642–10651.

37 L. Geng, Q. Li, C. Y. Meng, K. Dai, H. Y. Lu, C. S. Lin and W. D. Cheng, *J. Mater. Chem. C*, 2015, **3**, 12290–12296.

38 M.-L. Liang, C.-L. Hu, F. Kong and J.-G. Mao, *J. Am. Chem. Soc.*, 2016, **138**, 9433–9436.

39 S. D. Nguyen, J. Yeon, S.-H. Kim and P. S. Halasyamani, *J. Am. Chem. Soc.*, 2011, **133**, 12422–12425.
40 Y. Hu, C. Wu, X. Jiang, Z. Wang, Z. Huang, Z. Lin, X. Long, M. G. Humphrey and C. Zhang, *J. Am. Chem. Soc.*, 2021, **143**, 12455–12459.
41 H. S. Ra, K. M. Ok and P. S. Halasyamani, *J. Am. Chem. Soc.*, 2003, **125**, 7764–7765.
42 X.-L. Cao, C.-L. Hu, F. Kong and J.-G. Mao, *Inorg. Chem.*, 2015, **54**, 3875–3882.
43 J. Y. Chung, H. Jo, S. Yeon, H. R. Byun, T.-S. You, J. I. Jang and K. M. Ok, *Chem. Mater.*, 2020, **32**, 7318–7326.
44 (*a*) M.-L. Liang, Y.-X. Ma, C.-L. Hu, F. Kong and J.-G. Mao, *Chem. Mater.*, 2020, **32**, 9688–9695; (*b*) L. Lin, X. Jiang, C. Wu, L. Li, Z. Lin, Z. Huang, M. G. Humphrey and C. Zhang, *ACS Appl. Mater. Interfaces*, 2020, **12**, 49812–49821.
45 H. Liu, Q. Wu, X. Jiang, Z. Lin, X. Meng, X. Chen and J. Qin, *Angew. Chem., Int. Ed.*, 2017, **56**, 9492–9496.
46 J. Chen, C.-L. Hu, X.-H. Zhang, B.-X. Li, B.-P. Yang and J.-G. Mao, *Angew. Chem., Int. Ed.*, 2020, **59**, 5381–5384.
47 H. Yu, M. L. Nisbet and K. R. Poeppelmeier, *J. Am. Chem. Soc.*, 2018, **140**, 8868–8876.
48 H. Fan, C. Lin, K. Chen, G. Peng, B. Li, G. Zhang, X. Long and N. Ye, *Angew. Chem., Int. Ed.*, 2020, **59**, 5268–5272.
49 L. Geng, C. Meng, H. Lu, Z. Luo, C. Lin and W. Cheng, *Dalton Trans.*, 2015, **44**, 2469–2475.
50 F.-F. Mao, C.-L. Hu, X. Xu, D. Yan, B.-P. Yang and J.-G. Mao, *Angew. Chem., Int. Ed.*, 2017, **56**, 2151–2155.
51 M. Zhang, X. Su, M. Mutailipu, Z. Yang and S. Pan, *Chem. Mater.*, 2017, **29**, 945–949.
52 M. Luo, F. Liang, X. Hao, D. Lin, B. Li, Z. Lin and N. Ye, *Chem. Mater.*, 2020, **32**, 2615–2620.
53 L. Lin, X. Jiang, C. Wu, Z. Lin, Z. Huang, M. G. Humphrey and C. Zhang, *Chem. Mater.*, 2021, **33**, 5555–5562.
54 C. Wu, L. Lin, X. Jiang, Z. Lin, Z. Huang, M. G. Humphrey, P. S. Halasyamani and C. Zhang, *Chem. Mater.*, 2019, **31**, 10100–10108.
55 L. Cao, M. Luo, C. Lin, Y. Zhou, D. Zhao, T. Yan and N. Ye, *Chem. Commun.*, 2020, **56**, 10734–10737.
56 H.-X. Tang, R.-B. Fu, Z.-J. Ma and X.-T. Wu, *Inorg. Chem.*, 2021, **60**, 17364–17370.
57 E. Ko, H. Jo and K. M. Ok, *Inorg. Chem.*, 2021, **60**, 7914–7921.
58 H. Jo, M. H. Lee and K. M. Ok, *Chem. Mater.*, 2021, **33**, 1875–1882.
59 J. C. Hancock, M. L. Nisbet, W. Zhang, P. S. Halasyamani and K. R. Poeppelmeier, *J. Am. Chem. Soc.*, 2020, **142**, 6375–6380.
60 M. D. Donakowski, R. Gautier, H. Lu, T. T. Tran, J. R. Cantwell, P. S. Halasyamani and K. R. Poeppelmeier, *Inorg. Chem.*, 2015, **54**, 765–772.
61 M. R. Marvel, J. Lesage, J. Baek, P. S. Halasyamani, C. L. Stern and K. R. Poeppelmeier, *J. Am. Chem. Soc.*, 2007, **129**, 13963–13969.
62 J. B. Huang, S. Guo, Z. Z. Zhang, Z. H. Yang and S. L. Pan, *Sci. China Mater.*, 2019, **62**, 1798–1806.
63 H. Zhang, M. Zhang, S. Pan, X. Dong, Z. Yang, X. Hou, Z. Wang, K. B. Chang and K. R. Poeppelmeier, *J. Am. Chem. Soc.*, 2015, **137**, 8360–8363.
64 X. Chen, H. Jo and K. M. Ok, *Angew. Chem., Int. Ed.*, 2020, **59**, 7514–7520.
65 X. Chen, Q. Jing and K. M. Ok, *Angew. Chem., Int. Ed.*, 2020, **59**, 20323–20327.
66 Q.-R. Shui, R.-B. Fu, Z.-Q. Zhou, Z.-J. Ma, H.-X. Tang and X.-T. Wu, *Chem.–Eur. J.*, 2021, **28**, e202103687.
67 X.-L. Cao, C.-L. Hu, X. Xu, F. Kong and J.-G. Mao, *Chem. Commun.*, 2013, **49**, 9965–9967.
68 L. Liu, B. Zhang, P. S. Halasyamani and W. Zhang, *J. Mater. Chem. C*, 2021, **9**, 6491–6497.
69 H. Zhao, P. Gong, X. Zhang, Z. Lin, Z. Hu and Y. Wu, *Dalton Trans.*, 2020, **49**, 14046–14051.
70 F. You, F. Liang, Q. Huang, Z. Hu, Y. Wu and Z. Lin, *J. Am. Chem. Soc.*, 2019, **141**, 748–752.